High resolution digital outcrop model of the faults, fractures, and stratigraphy of the Agardhfjellet Formation cap rock shales at Konusdalen West, central Spitsbergen

Peter Betlem [a,b]**, Thomas Birchall** [a]**, Gareth Lord** [a]**, Simon Oldfield** [c]**, Lise Nakken** [a, b, d]**, Kei Ogata** [e]**, and Kim Senger** [a]

[a]Department of Arctic Geology, The University Centre in Svalbard, P.O. Box 156, N-9171 Longyearbyen, Svalbard, Norway

[b]Department of Geosciences, University of Oslo, Sem Sælands vei 1, 0371 Oslo, Norway

[c]Danish Offshore Technology Centre, Technical University of Denmark, Elektrovej, Building 375, 2800 Kgs. Lyngby, Denmark

[d]Department of Earth Sciences, Royal Holloway, University of London, Egham Hill, Egham TW20 0EX, United Kingdom

[e]Department of Earth, Environmental and Resource Sciences, Università degli Studi di Napoli Federico II, Via vicinale cupa Cintia 21, Complesso Universitario di Monte S. Angelo, Edificio L, 80126 Napoli, Italy

Correspondence: Peter Betlem (BetlemTech@outlook.com)

Abstract. Structure-from-motion (SfM) photogrammetry has become an important tool for the digitalisation of outcrops as digital outcrop models (DOMs). DOMs facilitate the mapping of stratigraphy and discontinuous structures like folds, faults and fractures from cm to km scale. With pristine, treeless exposures, the outcropping strata in Svalbard, Arctic Norway, hold exceptional potential for analogue studies and are ideally suited for the acquisition of high-resolution DOMs. We here present the acquisition, processing and integration of the Konusdalen West digital model data set, comprising both DOM and derived digital terrain model (DTM) data. Drone-based image acquisition took place over two weeks in July and August 2020. The Konusdalen West DOM and DTM cover a 0.12 km^2 area and span a 170 m elevation difference. The DOM covers the upper two-third of the mudstone-dominated Late Jurassic-Early Cretaceous Agardhfjellet Formation. The Agardhfjellet Formation and its time-equivalents are regional cap rocks for CO_2 sequestration and petroleum accumulations on the Norwegian Continental Shelf. Fifteen differential GNSS control points were used to georeference and quality assure the digital data assets, five of which functioning as reference checkpoints. SfM processing of 5512 acquired images resulted in high-confidence, cm-scale resolution point clouds, textured mesh (DOM), tiled model, orthomosaics, and a DTM. The confidence-filtered dense cloud features an average inter-point distance of 1.57 cm and has an average point density of 3824.9 points m^{-2}. The five checkpoints feature root mean square errors of 2.0 cm in X, 1.3 cm in Y, 5.2 cm in Z, and 5.7 cm in XYZ. Increased confidences and densities are present along the western flank of the Konusdalen West outcrop, where a fault-fracture network in mudstone-dominated strata is best exposed and photographed most extensively. Top and side-view orthomosaics feature maximum resolutions of 8 mm per pixel, enabling the mapping of faults, formation members, marker beds, fractures and other sub-cm features. Additional structural measurements and observations were taken in June 2021 to place the data in the geological context. Data described in this manuscript can be accessed at Norstore under https://doi.org/10.11582/2022.00027 (Betlem, 2022b).

1 Introduction

Structure-from-motion (SfM) photogrammetry has become an cost- and time-effective tool for the digitisation of outcrops (e.g., James et al., 2019; Westoby et al., 2012; Dering et al., 2019). SfM photogrammetry provides a means to digitally preserve outcrops and generate outcrop-truthed, georeferenced spatial data as digital outcrop models (DOMs) (Westoby et al., 2012; Burnham et al., 2022).

Outcrop analogue studies have supported subsurface developments by the petroleum industry and underground waste storage (e.g., CO_2, nuclear waste, gas) for several decades (Howell et al., 2014; Marques et al., 2020). Subsurface data often suffer from non-uniqueness, i.e., loosely constrained solutions based on data that are often sparsely and unevenly distributed. In

areas of good exposure, outcrop analogue studies provide high resolution data with significantly better spatial constraints and absolute spatial scales (Vollgger and Cruden, 2016). Outcrop-based mapping of stratigraphy and structures like folds, faults, and fractures from cm to km scale is therefore pertinent to understanding geological processes, not least those affecting storage and sealing capacity (e.g., Ogata et al., 2014, 2012; Sibson, 1996; Vollgger and Cruden, 2016; Ogata et al., 2023;
5 Betlem et al., 2023). Through SfM photogrammetry, outcrops can be digitised to scale and geospatially referenced as DOMs to facilitate quantitative interpretation and integration with other spatial data sets (e.g., quantifying fracture orientation and spacing; (Senger et al., 2015; Betlem et al., 2023)).

Extensive methodological reviews on the application of SfM photogrammetry ~~are~~ performed by, amongst others, Westoby et al. (2012), Smith et al. (2016), Dering et al. (2019) and James et al. (2019), often implementing unmanned aerial vehicles
10 (UAVs). SfM photogrammetry has been implemented to address a range of geomorphic (e.g., Leon et al., 2014; Rippin et al., 2015; Tonkin et al., 2016), sedimentary (e.g., Bilmes et al., 2019; Harrald et al., 2021) structural questions (e.g., Mulrooney et al., 2018; Vollgger and Cruden, 2016), and even on other planets (e.g., Barnes et al., 2018) and in analogue (laboratory scale) models (e.g., Donnadieu et al., 2003).

Despite the increased implementation of DOMs, most data and interpretations remain inaccessible (Vieira et al., 2021;
15 Burnham et al., 2022). Few repositories, such as V3Geo (Buckley et al., 2022) and e-Rock (Cawood and Bond, 2019) enable the sharing of DOMs, yet do not openly share the input data (e.g., photographs) and processing parameters, neither typically abide by FAIR (Findable, Accessible, Interoperable, Reproducible) principles for the complete datasets (Wilkinson et al., 2016). The recently published Svalbox Digital Model Database (Svalbox DMDb) has taken the next step to FAIR publishing of DOM data, and implements many of the FAIR principles to provide full, open access to input, processing and output data
20 alike (Betlem et al., 2023). FAIR and open-accessibility is essential for the reproducibility and re-evaluation of existing work, the application of new methodologies, future studies of temporal processes (e.g., weathering and climatic variation), and the conservation of geological sites as digital replicas (Burnham et al., 2022; Betlem et al., 2023).

This manuscript forms an important technical contribution to the digitalisation of outcrops as it outlines the best-practices learned from the Svalbox DMDb (Betlem et al., 2023) and makes these available to the geoscientific community as a state-of-
25 the-art example. Specifically, we present the acquisition, processing and integration of the Konusdalen West digital model data set, including a high-resolution, georeferenced DOM and orthomosaics covering the faulted, mudstone-dominated Agardhfjellet Formation in Svalbard, Arctic Norway. Finally, we discuss data availability, and provide ways to spatially interact with the digital data assets by integrating them with the Svalbox DMDb and visualising the textured mesh through the SketchFab and V3Geo online viewers.

1.1   The study area and outcrop geology

The High Arctic archipelago of Svalbard (Fig. 1) is part of the uplifted north-western margin on the Barents Shelf (Henriksen et al., 2011). The outcropping strata range from the Archean to Quaternary in age and offer a wide range of lithologies and tectonic settings. The strata in Svalbard have been shaped by several orogenic events, including the West Spitsbergen Fold and Thrust Belt (WSFTB) in the Palaeogene. Early Cretaceous magmatism introduced a system of dykes and sills as well as lava
35 flows into the stratigraphy, whilst glaciations and periglacial events over the last 100 ka have shaped the present-day landscape and modern exposure patterns (Harland et al., 1997; Henriksen et al., 2011; Senger et al., 2014). Following the last ice ~~age~~, approximately two-thirds of the archipelago remains covered by glaciers, with the remainder affected by periglacial processes, permafrost and featur~~ing~~ almost no vegetation (Humlum et al., 2003).

Petroleum and coal exploration boreholes have contributed significantly to our understanding of the stratigraphic evolution
40 of both Svalbard and the greater Barents Shelf (Senger et al., 2019). The Longyearbyen CO_2 Lab drilled eight fully cored wells in central Spitsbergen to assess a heavily fractured Mesozoic reservoir and cap rock, comprising the Wilhelmøya Subgroup and Janusfjellet Subgroup, respectively. The drilling provided wireline, stratigraphic, petrophysical, geophysical, and geochemistry data (Olaussen et al., 2019, and references therein), yet current top seal integrity remains difficult to ascertain with borehole data alone (Birchall et al., 2020; Huq et al., 2017). Geological constraints and inputs are needed to ascertain what may happen
45 following injection. The Konusdalen West outcrop, covering the lower part of the cap rock, is ideally suited for this and forms an important analog to assess the impact of faults and fractures on fluid flow in mudstone-dominated sequences (e.g., Ogata et al., 2012).

The fractured reservoir sections targeted by the Longyearbyen CO_2 Lab belong to the Upper Triassic to Middle Jurassic Kapp Toscana Group. The sandstone-dominated De Geerdalen Formation and overlying Wilhelmøya Subgroup represent paralic and
50 deltaic depositions, respectively (Mulrooney et al., 2018). These are overlain by 450 m-thick, regional, shale-dominated cap rock succession belonging to the Janusfjellet Subgroup (Koevoets et al., 2019; Braathen et al., 2012; Olaussen et al., 2019). The Janusfjellet Subgroup comprises the Late Jurassic-Early Cretaceous Agardhfjellet and Early Cretaceous Rurikfjellet formations (Collignon and Hammer, 2012; Dypvik et al., 1991; Grundvåg et al., 2017; Mørk et al., 1999; Koevoets et al., 2019).
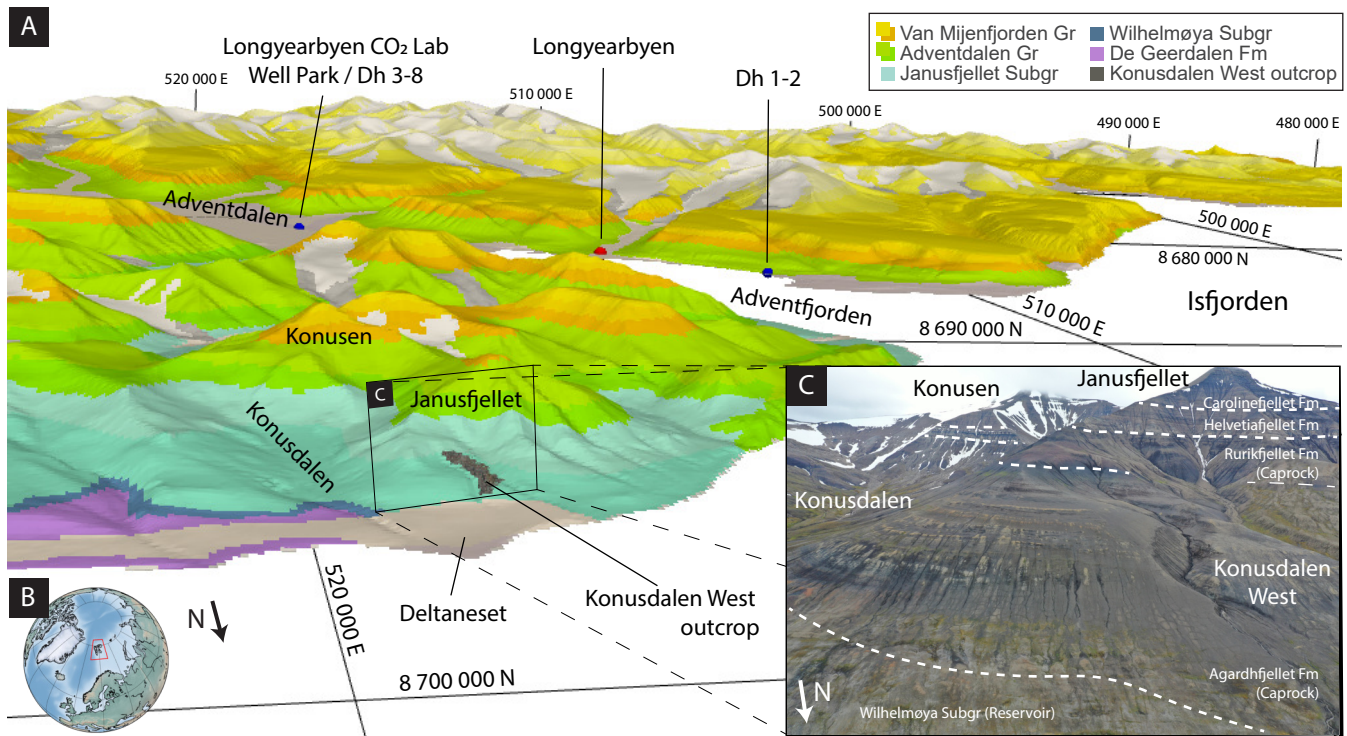
Figure 1. Location and geology of the Longyearbyen CO₂ Lab reservoir, cap rock and overburden successions in Svalbard (B). The locations of the outcropping Konusdalen West exposures at Deltaneset, the city of Longyearbyen, and both drill sites of the Longyearbyen CO₂ Lab are highlighted. The inset (C) shows an overview photo of the study area. Geological map (1:250 000) and digital terrain model (50 m resolution) are courtesy of Norwegian Polar Institute (2014) and Norwegian Polar Institute (2016).

The Agardhfjellet Formation was formed mostly under dysoxic to anoxic conditions, periodically experiencing oxygenation of the water column (Collignon and Hammer, 2012). It forms the cap rock immediately overlying the targeted reservoir of the Longyearbyen CO₂ Lab and crops out at Deltaneset, some 15 km north-west of Longyearbyen (Fig. 1) (Braathen et al., 2012; Olaussen et al., 2019). Here, the cap rock is host to several potential seal bypass systems, including igneous and sedimentary intrusions, faults and folds, that may affect the flow of fluids through the cap rock (e.g., Ogata et al., 2023; Betlem et al., 2023; Betlem, 2023a, and references therein). Time-equivalent stratigraphic intervals of the Agardhfjellet Formation are widespread across the Barents Sea and are prolific regional source rocks, in addition to being the top seal of several oil and gas fields on the Norwegian continental shelf (e.g., Spencer et al., 2008).

Within our study area, the Agardhfjellet Formation is up to 250 m thick and can be subdivided into four member units (Dypvik et al., 1991; Koevoets et al., 2018, 2019). The Oppdalen Member is a fining-upward unit of Bathonixian-Oxfordian age, deposited in a shallow-marine environment. The Lardyfjellet Member overlies the Oppdalen Member and consists of black paper shales with scattered carbonate concretions. The first appearance of silt-sand beds and disappearance of black shales marks the transition into the Oppdalssåta Member. The Upper Kimmeridgian Oppdalssåta Member comprises several upward-coarsening sandstone and sandy shale units, of which the last marks the end of the member. The Slottsmøya Member (Lower Volgian-Ryazanian) consists of black paper shales, developing slightly coarsening-upwards sequences in the upper part.

The Paleocene-Eocene evolution of the West Spitsbergen Fold and Thrust Belt (WSFTB) resulted in a series of eastward-transported thrust sheets rooted in sub-horizontal decollement zones along weaker evaporite and shale intervals, including the Agardhfjellet and Rurikfjellet formations (Ogata et al., 2012). Considerable lateral variation of the formation is observed throughout Spitsbergen, both in total thickness and in the relative thicknesses of its members. Tectonic disturbances of the mechanically weak Agardhfjellet Formation are likely to have occurred through the WSFTB (Braathen et al., 1995; Bergh et al., 1997).

The Rurikfjellet Formation features several coarsening-upward units, deposited in a marine shelf to prodeltaic and shoreline delta-front environment (Dypvik et al., 1991; Grundvåg et al., 2017). Transition from the Agardhfjellet Formation into the Rurikfjellet Formation is marked by the Myklegardfjellet Bed, a distinct and easily observable clay unit (Dypvik et al., 1991).

2 Methods

2.1 UAV surveying

UAV-based acquisition of the outcrop was conducted over two weeks in July and August 2020. We used a DJI Mavic 2 Pro drone with a Hasselblad L1D-20c camera (10.26 mm focal length; 20 MP images) with built-in GNSS positioning to image the
5 Konusdalen West outcrop at a mean flight altitude of 30.62 m (median 29.8, std. 5.72 m). Maximum flight velocity was kept at 1.1 m s^{-1} with image acquisition triggered automatically at 5 second intervals and resulting in 5512 images (Fig. 2, Table A1).

2.2 Ground control points and structural location measurements

Fifteen control points were laid out around the eastern slope of the best-exposed part of the Konusdalen West outcrop (Fig. 2). Control point locations were measured prior to the UAV survey in August 2020 using a LEICA Viva GS16 receiver with LEIGS
10 antenna (pole length: 1.800 m). Each location was measured for at least 30 seconds and calibrated against the long observation base station in Longyearbyen ("LYRS"; TRIMBLE NETR9 receiver with TRM41249.00 antenna), approximately 15 km south-west of the study area (78° 13' 43.77" N, 15° 23' 50.32" E, and 495.682 m WGS84 ellipsoidal height; 509048.1382 E, 8683937.5685 N, and 463.4025 m orthogonal height [WGS84/UTM Zone 33N with Earth Gravitational Model 2008, EGM2008]) using a post-processing static approach. Post-processing performance of the Leica Viva GS16 system is rated
15 at 3 mm + 0.1 ppm horizontal and 3.5 mm + 0.4 ppm vertical accuracy (Leica Geosystems AG, 2016). This translates to an overall accuracy at the targeted field site of +- 1.8 mm horizontally and +- 9.5 mm vertically. One-second interval base station data were retrieved through ftp.statkart.no in the RNX2 and RNX3 formats. The Leica Infinity software package (v3.6.0.35318; 64bit) was used for processing, implementing EGM2008 (Pavlis et al., 2008) for the calculation of orthogonal heights from the measured WGS84 ellipsoidal heights. In accordance with the guidelines proposed by Dering et al. (2019) and James et al.
20 (2019), ten markers were used as ground control points (GCPs) for calibration of the point cloud. The remaining five were used as check points (CPs).

The use of ArUcO markers enabled the automated analysis and control point-detection in the images by using the OpenCV ArUcO library (Bradski, 2000; Garrido-Jurado et al., 2014). The automated_metashape package (v1.1.10, Betlem, 2022a) streamlined the integration thereof with Agisoft Metashape through use of the Metashape Python API. The ArUcO markers
25 implemented the DICT_6X6_250 encoding. Each automated control point marker placement was subsequently checked and where needed manually refined to ensure the highest precision and accuracy.

We measured additional fault and fracture orientation data by handheld-compass in June 2021. The measurements followed excavation of up to half a metre of material and were located with the Leica Viva GS16 system. The structural measurements supplement and constrain digital annotations and provide additional surface elevation reference data.
30 All recorded coordinates are provided in Table 1 and Table C1, including model errors, using the WGS84/UTM Zone 33N coordinate system (EPSG:32633) and orthogonal heights (altitudes) derived from EGM2008 (Pavlis et al., 2008).

2.3 Point cloud, orthophoto mosaic and digital outcrop models

Image processing and surface reconstruction were performed using Agisoft Metashape (formerly PhotoScan, v1.7.2.12040). Metashape is a commercial software that implements automatic feature detection, image matching and modelling using SfM
35 algorithms, and is frequently used for model reconstruction (e.g., Tinkham and Swayze, 2021; Zhou et al., 2020; Kingsland, 2020). Agisoft does not disclose the exact algorithms used in the processing, but does refer to Hirschmuller (2007) and Hiep et al. (2009).

Processing was performed in local area network (LAN)-mode on six dedicated workstations (Table B1) and proceeded according to the latest USGS coastal imagery processing guidelines (Over et al., 2021). For a schematic summary of the steps
40 involved, the reader is referred to Fig. 1 in Over et al. (2021). Minor deviations from the workflow and processing parameters are discussed below.

We quality controlled all images prior to processing and additionally used Metashape's inbuilt image assessing tool to quantify image quality. Four images did not pass the specified cutoff of 0.5 and were disabled. Image location metadata for flight 23-25 featured erroneous altitude data in excess of 100 m above the recorded flight paths. Location metadata for these
45 images (n = 748) were disabled prior to the photo alignment step. The sparse point cloud was generated using the highest setting (i.e., four times upscaled image) through two consecutive iterations to re-align any non-aligned images, leaving four unaligned. Subsequent camera optimization only utilized the high-precision GCP data, disabling all image location metadata and unpinned (implicit, "blue flags") GCP points to ensure the most accurate georeferencing. Tie points were filtered on reconstruction uncertainty (level = 15, one optimization, removed 16 021 109 points, disabled four cameras), projection accuracy (level = 2,
50 one optimization, removed 2 497 962 points, disabled three cameras) and reprojection error (level = 0.3, seven optimizations,

removed 4 650 001 points, disabled two cameras). A camera alignment-optimization step followed each filtering step. The depth maps and dense point cloud were processed using the half-image scale and applied "mild" filtering of the generated depth maps. No changes were made to the automatically-generated bounding box.

The dense cloud was trimmed based on confidence (retaining 10<= point confidence, removed 1 034 950 382 points) to improve overall quality. The trimmed dense cloud featured as input for the generation of a (textured) mesh, tiled model, and digital terrain model (DTM). Contours were extracted from the DTM at 5 m steps across the 85-255 m interval. The mesh and DTM were used for the generation of several orthomosaics, including top-down and viewpoints aligned with the key geological features of interest. A processing report detailing additional processing parameters is made available as part of the data set (Betlem, 2022b).

2.4 Point cloud, vertex and data operations

We analysed point cloud and mesh data using Python's Point Data Abstraction Library, PDAL (PDAL Contributors, 2018; Butler et al., 2021, v. 2.2.0/2.4.2 (python-pdal)). Point cloud data were exported as single .LAS files, while mesh data was PDAL-converted from the .obj file format to the .LAS file format. Point cloud and mesh data were subsequently split into one m^2 bins from the (500000, 8680000) grid origin using the PDAL-splitter filter. Points per bin, extent, and bin centres were calculated for both tie points and dense cloud data. Mean confidence was additionally calculated for each m^2 binned interval. Outlines were calculated with PDAL's hexbin filter, specifying an *edge_length* of 0.6204 units (m). Slopes and aspects were calculated from the DTM data through use of OSGeo and GDAL/OGR (Rouault et al., 2022, v. 3.2.1). Functional scripting examples are found in the digital appendix, and include point and vertex density, boundary estimate, and error calculations.

2.5 Delineation and structural measurements of geological features in the point cloud and digital terrain models

Metre-scale geological features were interpreted as georeferenced 3D features on the dense point cloud, textured mesh and tiled model through use of Metashape's built-in polygon tool. Published sedimentary logs (Koevoets et al., 2018, 2016) helped with the integration of the model into its geological context and aided the placement of formation and member boundaries. Marker beds and faults were traced only where clearly visible along the entire DOM and confirmed in the field. Fracture sets were analysed and classified through use of the NetworkGT software (Nyberg et al., 2018). Dip angles were calculated from the interpolated planes through line traces with at least 3 points, i.e., 3D data. The same methodology was applied to along-fault groupings of dGNSS field measurements (Table C1) to obtain interpolated fault planes and structural information.

2.6 Accuracy assessment and mis-alignment

Accuracy assessment implemented the error associated with the geometric accuracy of the dense cloud and digital terrain model (DTM). We calculated mean and Root-mean-square errors (RMSE) for both the GCPs and CPs and employed differential augmentation of the global navigation satellite system (dGNSS) to constrain the lateral and vertical accuracy of the DTM at the control points. The altitude-DTM difference was in addition calculated for dGNSS data recorded for structural measurements and against available 5 m-resolution DTM reference data (Norwegian Polar Institute, 2014).

2.7 Visualisation and data integration

We employed the WGS 84/UTM zone 33N (EPSG:32633) projection. The Norwegian Polar Institute provided geological maps with 1:250 000 and 1:100 000 scales (Norwegian Polar Institute, 2016). We used Python's Bokeh, HoloViews (Stevens et al., 2015) and Scientific colour maps 7.0 (Crameri et al., 2020) libraries for the visualisation of the data as georeferenced maps. Given computational and file-size limitations, the DTM, aspect, slope, and orthomosaic data were downsampled prior to visualisation. In line with file-size limitations and publishing policy, a decimated copy of the textured mesh (5 M faces) was filtered on connected component size (99%) prior to submission to V3Geo and SketchFab.

3 Results and Discussion

3.1 Point clouds and control points

The initial tie point set (i.e., sparse cloud) consists of 29 492 561 points following camera alignment, trimmed to 6 323 579 points through error-reducing camera optimization steps (Fig. 3). Tie point multiplicity, i.e., the average number of images where the point has been measured, of the processed point cloud is calculated as 3.81. The processed sparse cloud features an RMSE reprojection error value of 0.12 pixels and a max reprojection error of 0.88 pixels.

The full-extent dense point cloud (Fig. 4) consists of 1 543 094 332 points and features an average point-to-point distance of 1.26 cm and 6222 points m^{-2} density (std. 4767 points m^{-2}), covering a total area of 0.245 km^2. Full-extent dense cloud confidence ranges from 1 to 194, with confidence values above 9 considered high.

Point exclusion of low-confidence points led to an improvement in mean confidence from 12.92 (std. 19.83) to 34.54 (std. 22.1) for the reduced dense cloud (508 143 950 points), mainly through the removal of points closer to the edges of the surveyed area (Fig. 4). The filtered dense cloud has an average point-to-point distance of 1.57 cm and features an average point density of 3824.9 points m^{-2} (std. 2215.4 points m^{-2}).

The spatial accuracy of the point cloud was assessed using five independent CPs, disabled during point cloud generation and camera optimization (Table 1). All GCPs and CPs besides GCP 15 and CP 02 featured a post-processed phase fixed point solution, i.e., *Fixed PP*. Post-processing of GCP 15 and CP 02 resulted in less accurate code solutions, i.e., *Code PP*. Overall CP RMSE is 1.96 cm in X, 1.31 cm in Y and 5.17 cm in Z, with the overall XYZ error calculated at 5.69 cm (mean: 5.24 cm, std.: 2.46 cm). Slightly larger errors were observed for the GCPs (Table 1). Overall GCP RMSE of the ten points is 3.01 cm in X, 6.37 cm in Y and 21.80 cm in Z, with the overall XYZ error at 22.90 cm (mean: 11.60 cm, std.: 20.82 cm). Removal of 2-sigma outliers, i.e., GCP 2, lowered the RMSE to 9.76 cm (mean: 5.53 cm, std.: 8.53 cm), bringing the calculated errors in line with the RMSE XYZ error calculated for the CPs.

Table 1: Ground control points (GCPs) and Check points (CPs) used for high-resolution georeferencing. Easting and Northing given in the epsg:32633 reference system. Heights are the calculated ortho heights using Earth Gravitational Model 2008 (Pavlis et al., 2008).

Marker	Type	Images	Northing (y, m)	Easting (x, m)	Altitude (m)	Error (x, cm)	Error (y, cm)	Error (z, cm)	Error (xyz, m)	DTM (m)	Alt.-DTM (cm)
01	GCP	89.0	8696183.479	518772.856	192.404	6.222	1.579	0.822	6.471	192.417	-1.378
02	GCP	115.0	8696265.172	518742.048	188.769	1.832	-5.680	-65.981	66.250	188.103	66.605
03	GCP	88.0	8696342.463	518709.156	170.5	-0.049	-0.434	-0.268	0.513	170.503	-0.341
04	GCP	58.0	8696416.147	518713.526	151.964	-1.561	-0.447	-1.440	2.171	151.953	1.096
07	GCP	70.0	8696450.708	518744.881	120.22	0.080	0.958	-2.179	2.382	120.195	2.409
10	GCP	61.0	8696516.925	518722.178	129.467	-0.120	0.187	3.329	3.337	129.544	-7.659
11	GCP	60.0	8696538.309	518742.953	108.885	0.346	0.538	-4.529	4.574	108.851	3.435
12	GCP	74.0	8696500.905	518754.466	104.902	0.093	-0.754	-0.225	0.793	104.9	0.138
14	GCP	48.0	8696271.709	518797.111	163.658	-0.164	0.292	-1.765	1.797	163.633	2.570
15	GCP	83.0	8696214.39	518819.154	180.902	6.781	-19.185	18.846	27.735	181.002	-10.029
Mean	GCP	74.6	-	-	-	1.346	-2.295	-5.339	11.602	-	5.685
Mean (excl. GCP 02)	GCP	70.111	-	-	-	1.292	-1.918	1.399	5.530	-	-1.084
RMSE	GCP	-	-	-	-	3.011	6.365	21.797	22.906	-	21.501
RMSE (excl. GCP 02)	GCP	-	-	-	-	3.115	6.436	6.646	9.762	-	4.554
Std.	GCP	19.699	-	-	-	2.839	6.258	22.276	20.818	-	21.858
Std. (excl. GCP 02)	GCP	14.487	-	-	-	3.006	6.517	6.891	8.532	-	4.692
05	CP	104.0	8696343.978	518747.921	151.448	-3.426	2.062	3.625	5.398	151.485	-3.733
06	CP	68.0	8696405.441	518747.357	131.928	1.940	-0.344	-5.441	5.787	131.888	4.036
08	CP	113.0	8696459.538	518723.651	137.547	-0.485	1.759	5.299	5.604	137.603	-5.546
09	CP	81.0	8696492.032	518739.179	129.011	-0.495	-0.417	-1.142	1.312	128.996	1.511
13	CP	56.0	8696242.35	518788.954	178.719	1.781	0.982	-7.857	8.116	178.658	6.113
Mean	CP	84.4	-	-	-	-0.137	0.808	-1.103	5.243	-	0.476
RMSE	CP	-	-	-	-	1.957	1.312	5.174	5.685	-	4.486
Std.	CP	23.923	-	-	-	2.183	1.155	5.652	2.457	-	4.987

The sparse and dense point clouds featured very high point densities near control points and across steeper terrain intervals. Both are partly biased by the here-employed sampling and processing methods. Neither, however, affect the quality of the model following the confidence-enhancing processing steps. Firstly, control points feature increased point densities as additional photographs were taken to streamline and improve automated-marker detection, i.e., sampling bias. Secondly, the method of reporting point densities along the horizontal plane does not properly account for (sub-)vertical features, where points follow a vertical rather than horizontal distribution in three-dimensional space. Cliff sections and steeper slopes, for instance, thus appeared more pronounced in the horizontal dense point cloud density projections, though did not actually contain a higher point density, as also evident from manual inspections.

Areas further away from the best-exposed, eastern slope of the Konusdalen West outcrop generally featured lower point densities. The southernmost part, for example, features a lower imaging-density than the densely photographed eastern side (Fig. 2). The density-drop in the south-west is similarly caused by a lower imaging-density. Decreased point densities were also observed on the shadow sides of obscuring features. Overall camera obscurement, however, remained minimal, being very localised and often smaller than 0.25 m^2 and well below the 1 m^2 area used for binned interval calculations shown in Fig. 3 and ~~Fig.~~ 4. The occurrence of rocks and boulders provides additional data on the composition and mechanical stability of the slope. Such data may also be of use to researchers from other disciplines enabling better integration of future multi-disciplinary workflows.

3.2   Digital terrain model, outcrop model, and orthomosaics

The textured mesh features a mean vertex density of 395.29 vertices m^{-2}, a factor of 10 lower than recorded for the dense cloud and covers an area of 0.12 km^2 (Fig. 5). Vertex density ranges from 1 to 3458 vert. m^{-2} (std. 150.89 vert. m^{-2}), with higher values observed in parts corresponding to steeper sections and more competent lithologies with higher quartz content. Vertex density and resolution are more than sufficient for digital annotation and quantitative measurements of the outcrop.   5

Interpolation of the dense cloud enabled the generation of a DTM (Fig. 6) with a 1.6 cm/pixel resolution. The DTM features a range in elevation from 84.36 m to 256.23 m. For evaluating the elevation accuracy of the DTM, elevations were compared with the GPCs/GCs, structural measurement locations obtained by dGNSS (Table 1), and existing DTM data available from the Norwegian Polar Institute (i.e., the "reference", Norwegian Polar Institute, 2014). Point altitude/DTM differences range from -10.03 cm to 66.61 cm (3.44 cm, excluding outliers) for the GCPs and -5.55 cm to 6.11 cm for the CPs. GCPs feature a mean   10 altitude-DTM error, standard deviation and RMSE of 5.69 (-1.08) cm, 21.86 (4.70) cm and 21.50 (4.56) cm, respectively, when compared to the here-generated DTM, with the error in brackets stemming from outlier removal, i.e., GCP 02. CPs feature a mean altitude-DTM error, standard deviation and RMSE of 0.48 cm, 4.99 cm and 4.49 cm, respectively.

An additional 72 points were measured to constrain fault locations and orientations in the outcrop, so-called ground-truthing points (Table C1; Fig. 2). Post-processing of the points led to 19 *Code PP*, 17 *Widelane PP*, and 36 *Fixed PP* solutions,   15 with *Widelane PP* being slightly less accurate than *Fixed PP* solutions (Table C1). Altitude comparison with the DTM yields absolute mean errors of between 1.19 cm and 16.59 cm. Accompanying RMSE errors show a larger spread, ranging from 1.37 m for *Code PP* to 0.22 m for *Fixed PP* solutions. As also for the control points, errors are largest in the lowermost part of the outcrop close to the stream, where GNSS coverage is affected by horizon obstruction in the gulley. The ground-truthing points show larger errors than those recorded for the GCPs/CPs. Measured a year after the UAV survey, the error-difference may be   20 indicative of geological processes (e.g., active layer freeze-thaw) acting on the outcrop, as also evidenced from the comparison with the published 5 m-resolution DTM reference (Norwegian Polar Institute, 2014).

The Konusdalen West DTM differs on average by +0.927 m (std. 0.38 m) from the reference (Fig. 6). The largest positive deviations (<5.11 m) are observed along the steepest section at the outcrop's eastern side. A few negative deviations (>-0.73 m) are found towards the west. The differences fall within the 2 to 5 m range listed for the standard deviation of the reference   25 data set (Norwegian Polar Institute, 2014) and suggest both DTMs are in agreement.

The DTM is of high enough quality for the generation of slope and aspect maps (Fig. 6) and high resolution orthomosaics. The latter (e.g., Fig. 7 B, Fig. 9) complement the data package with view-specific resolutions of up to 8 mm per pixel, which is twice as detailed as available for the DTM. Fig. 7 B depicts the highest resolution afforded by the data package. Fractures and other observations up to sub-cm scales can be identified and annotated as georeferenced features.   30

The outline of the DTM visualises minor gaps in the data sets, including lower data coverage toward the edges of the model. The presence of two larger, low-density areas is also marked in Fig. 7 by interior polygons and is a result of insufficient image coverage due to operator selection of better exposure and manually-operated UAV flights.

Topographic challenges and the remoteness of the site prevented the use of autonomous drone missions. Like most of Svalbard, the study area does not have telecommunication coverage, ruling out internet-supported, advanced flight planning   35 services. Offline solutions exist, but do not adjust the flight path to account for elevation changes and require high-resolution terrain models to be available. The outcrop covers approximately 170 m of elevation difference and features several near-vertical sections next to a narrow gulley (Fig. 6), further complicating automation and consistency of image acquisition.

Few other low-confidence, low-point/vertex-density areas exist and are shared by all worked-up products, i.e, DTM, DOM, and orthomosaics. We deem these mainly a result of confidence-enhancing filtering steps that were applied to the tie points and   40 dense cloud, a necessity in the processing workflow to assure output accuracy.

Confidence and density remain highest in the area covered by GCPs/CPs, focused on by a higher proportion of flights. Even in areas affected by quality reductions, the data remain of sufficient quality for a quantitative assessment at lower resolutions, and inherently capture enough evidence for future users to have a realistic expectation of data availability.

4   Visualisation and integration   45

The high quality DOM data allow quantitative interpretation of the entire outcrop, including deciphering the sedimentological and structural evolution of the area. When combined with local geoscientific datasets and fault core architecture observations, the quantifiable data sets combine into a powerful tool that lends itself to detailed integrated studies of the outcrop.

4.1 Stratigraphic-structural integration

The Konusdalen West DOM spans the middle-upper successions of the Agardhfjellet Formation. The model covers the Slottsmøya, Oppdalssåta and Lardyfjellet members and displays internal bed characteristics in detail, as highlighted by Fig. 7 and Fig. 9. The stratigraphic boundaries and structural features have all been annotated directly on the digital model data. The points, lines and polygons are generated as fully georeferenced 3D data and can be easily exported, visualised and processed by other toolsets. A brief geoscientific integration is provided by the discussion that follows, an important aspect to the applicability of the geospatial annotations and data sets.

The lower limit of the outcrop sits atop a thick, inconspicuous succession of black shales beyond the lower limits of the model. At the very base of the DOM, a glauconitic bed and limestone concretions mark the transition from the Lardyfjellet to the Oppdalssåta members. Only the uppermost 10 m of the Lardyfjellet Member's succession of dark shale, siderite horizons and lenses are exposed and visible within the model (Dypvik et al., 1991; Mørk et al., 1999; Koevoets et al., 2018). The transition into the Oppdalssåta Member coincides with the start of a coarsening-upwards packages that span the lower half of the Konusdalen West outcrop. The coarsening-upwards shale, siltstone and sandstone packages come in 10 to 15 m-thick intervals. The member is considered to represent the coarsest grained interval of the Agardhfjellet Formation (Dypvik et al., 1991; Dypvik and Harris, 2001; Koevoets et al., 2018).

An approximately 10 m-thick black shale interval overlain by a 1 m-thick silty sandstone marks the transition into the Slottsmøya Member. The Slottsmøya Member consists of dark-gray to black-silty mudstone and discontinuous silty beds, including an abundance of siderite and dolomite interbeds and yellow-to-red sideritic concretions (Koevoets et al., 2018). The member can be separated into three parts, with their transitions demarcated by the Yellow Silty and Dorsoplanites Beds, both annotated in the Konusdalen West DOM and orthomosaics (Collignon and Hammer, 2012). The succession below the Yellow Silty Bed is dominated by siderite beds. The sequence above grades from a (paper) shale into a very-fine sandstone succession commonly abundant with ammonites, i.e., the Dorsoplanites Bed. The upper limit of the Konusdalen West DOM coincides with the Myklegardfjellet Bed and transition into the shales of the Rurikfjellet Formation.

Field and digital measurements identified at least two dozen, mainly northeast-southwest-trending normal and east-west antithetic faults within the Oppdalssåta and lower Slottsmøya members (Fig. 7 C, Fig. 9; Nakken (2020)). These orientations are consistent with faulting affecting the Wilhelmøya Subgroup reservoir and the Lardyfjellet and Oppdalen members of the Agardhfjellet Formation. Faulting in both sequences has been attributed to Palaeogene transpression during and following the evolution of the WSFTB (Mulrooney et al., 2018; Ogata et al., 2014). The Slottsmøya Member sequences up to the Dorsoplanites bed show evidence of strong shearing, exemplified by multiple detachment planes and numerous associated, steeply dipping thrust faults. The shear zone is a well-documented phenomenon in the upper Agardhfjellet and lower Rurikfjellet formations, one of two main detachment zones affecting the reservoir and cap rock of the Longyearbyen CO_2 Lab targeted reservoir-cap rock system (Ogata et al., 2014; Braathen et al., 1997; Bergh et al., 1997).

Exposed fault lengths vary between one metre and a few tens of metres, while offsets range from centimetre to decametre scale. Faults are generally disconnected, with the exception of a large, through-going fault that offsets a smaller, north-south striking fault by 8.5 m across the Oppdalssåta Member, Fig. 7 B. Continuation of the two faults into the lower half of the Slottsmøya Member is characterized by a splay-like structure that continues past the Yellow Silty Bed. Shallow excavation along the fault plane of the through-going fault provided insights into the thickness variations and heterogeneities within the fault core. Thickness increased with fault displacement and more competent host rock (up to 1.5 m). The fault core remained narrow (ø: < 10 cm) within intervals dominated by black shales.

4.2 Field and digital data across scales

With sub-cm scale resolutions, the digital data assets support the extraction of structural and sedimentological data across a range of scales. For instance, the fault plane can be traced in the DOM and orthomosaics even across the shale-rich intervals by identifying alterations of the surface. Orientations derived from this largely agree with those measured in the field (Fig. 7 C). Due to surface and scree cover, the fault core architecture itself remained inaccessible in the surface reconstructions. As in the field, the network of anastomosing shale gouge membranes, intensely fractured shale lenses, and fault breccia as seen in Fig. 8, were only visible across excavated cross-sections. Larger features, where exposed at the surface, could be distinguished from both field observations and digital assets alike. Iron-cemented carbonate lenses were found in the lower-middle sequences of the Oppdalssåta Member, where such beds are abundant. The lenses were oriented in an elongate manner parallel to the fault axis and were intensely fractured.

The digital and tiled models of the Konusdalen West outcrop are of high enough quality to map individual fractures with apertures smaller than 1 cm, as shown in Fig. 7 D-E. Open fractures and light-coloured, mineralized veins following lineaments are found throughout the digitised interval in three primary fracture sets, covering north-south, northeast-southwest and

northwest-southeast striking orientations. Digital fracture tracing enables the quantification, validation and modelling of these networks, as well as the extraction of orientations and fracture sets, Fig. 7, (Betlem et al., 2023). Although this contribution implemented the fracture analysis tool NetworkGT, other fracture analysis tools such as FracPaQ exist and have been used in this and similar settings (e.g., through FracPaQ, Healy et al., 2017; Rizzo et al., 2020, 2021). Fracture analysis facilitates a comprehensive appraisal of the fracture network and its associated permeability, capturing the intricate details of fracture size, density distribution and connectivity. Recent work by Rizzo et al. (2023) illustrates this potential, as it implements an earlier iteration of the Konusdalen West DOM to detail the extraction of quantitative data on the fault and fracture network across the lowermost cap rock. Specifically, Rizzo et al. (2023) integrated the DOM-derived fracture network with laboratory-based stress-permeability data to model upscaled permeability and fluid leakage potential across two windows in the outcrop, targeting the Slottsmøya Member splay-like structure and the silty cliff formers in the upper and lower part of the outcrop, respectively.

4.3 The Longyearbyen CO_2 Lab: DOMs and carbon sequestration

Digital outcrop analysis coupled with multiphysical data and laboratory measurements can be used to create accurate coupled geological models. The Konusdalen West DOM can be directly integrated with the data available through the Longyearbyen CO_2 Lab that include borehole and drill core data (Fig. 9) (Schaaf et al., 2017; Nakken, 2020; Løvlie, 2020; Ogata et al., 2012, 2014). The digital data assets further complement the extensive set of available fracture data that cover both the outcrop (e.g., Løvlie, 2020; Nakken, 2020; Ogata et al., 2014) and drill cores from the fully-cored cap-rock sequences (Ogata et al., 2014; Olaussen et al., 2019). This forms an ideal starting point for stratigraphic correlation at the bed-resolution that enable the generation of high-resolution, outcrop-truthed geomodels suitable for numerical modelling, the mapping of discretized fracture networks, appraisal of fluid flow, and the constraint of the damage zone around faults. These, in turn, can inform the design and operation of gas storage projects, enabling more effective containment strategies, improve risk assessments, and ultimately, lead to more successful storage initiatives. In this context, the Konusdalen West DOM is key to the appraisal of a regionally-important cap rock.

5 Data availability

The full Konusdalen West model, including input photographs, processing report, textured, tiled and surface models, can be freely downloaded from the Norwegian National Infrastructure for Research Data Research Data Archive (Norstore; https://doi.org/10.11582/2022.00027) (Betlem, 2022b). Visualisation and interpretation is possible through freeware (e.g., Agisoft's Viewer, Blender) and commercial software like LIME (Buckley et al., 2019) and VRGS (Hodgetts et al., 2015). Reduced-size textured models and corresponding metadata are available online through the Svalbox Digital Model Database (Betlem et al., 2023), SketchFab, and V3Geo (Buckley et al., 2022), Table 2.

The full dataset (Betlem, 2022b) consists of the following files and zipped archives:

- A representative overview image file of the outcrop;
- Processing reports in PDF and HTML format;
- data.zip archive containing input UAV imagery, including disabled photos, and input differential GNSS data, including GCP coordinates, field measurements and related errors;
- metashape.zip archive containing the Agisoft Metashape project featuring sparse and dense point clouds, mesh including textures, tiled model, DTM, and orthomosaics.
- export.zip archive containing exported DOM, DTM and orthomosaic data, as well as geopackages with delineation and structural measurements of geological features in epsg:32633 and local crs (epsg:4978).

The JupyterLab processing pages and examples have been uploaded to the Zenodo data repository under https://doi.org/10.5281/zenodo.10182529 (Betlem, 2023b).

Table 2: Overview of available data.

Data set	Comments	DOI/URL/Reference
Input photographs, output (DTM, DOM, orthomosaic), processing report, Agisoft Metashape project, (interpretation) shapes	Data package	Betlem (2022b)
JupyterLab processing pages	Processing example package	Betlem (2023b)
Digital outcrop model and metadata	Svalbox Digital Model Database. In context with other Svalbard geoscientific data.	Svalbox ID: Svalbox-DOM_2020-0039
(Reduced component) digital outcrop model	SketchFab viewer. Web-based platform with virtual reality options.	SketchFab ID: 9d89ed14050c4498910dad86944bbdea

Data set	Comments	DOI/URL/Reference
(Reduced component) digital outcrop model and metadata	V3Geo repository. Web-based platform with interpretation possibilities.	V3Geo ID: 391

6 Conclusion

We present high resolution digital models of the faulted, shale-dominated Agardhfjellet Formation cap-rock succession in Svalbard. The Konusdalen West digital outcrop model (DOM) has been ground-truthed via dGNSS and has been processed according to community standards to improve confidence and reduce errors. The digital models feature maximum resolutions of 8 mm per pixel and outlier-removed, overall spatial accuracies of less than 10 cm. The (textured) surface models and orthomosaics enable the deciphering of the sedimentological and structural evolution of the area, including the delineation of sub-cm scale features such as fractures. Areas of reduced quality stem mainly from operator selection of better exposures, i.e., the eastern and best-exposed part of the outcrop, and confidence-increasing processing. The quality of the otherwise pristine, faulted, mudstone-dominated outcrop is not affected. Further, the data captures the presence of obscuring features in high detail, which can be used to help constrain the composition and mechanical stability of the slope. The Konusdalen West model is suitable input for accurate, high resolution fracture mapping and geomodelling, especially when combined with available regional and Longyearbyen CO_2 Lab data sets. As time-equivalent stratigraphic intervals of the Konusdalen West outcrop are prolific regional source and cap rocks in the Barents Sea, the presented data are invaluable for structural, analogue, cap rock appraisal, and fluid flow studies.

7 Appendix

Table A1: Flight counts, image ids, counts and other acquisition metadata. Flight metadata for flights 23-25 were disabled owing to inaccurate altitude recordings.

flight	image-ids	image-count	disabled	non-aligned	flight-date	weather
flight-01	im_0001-im_0280	280	-	im_0278, im_0280	24-07-2020	overcast
flight-02	im_0281-im_0559	279	-	im_0410, im_0411	24-07-2020	overcast
flight-03	im_0560-im_0770	211	im_0763, im_0764, im_0765, im_0770	im_0749, im_0766, im_0767, im_0768, im_0769	24-07-2020	overcast
flight-04	im_0771-im_1035	265	-	-	25-07-2020	overcast
flight-05	im_1036-im_1312	277	-	-	25-07-2020	overcast
flight-06	im_1313-im_1564	252	-	-	25-07-2020	overcast
flight-07	im_1565-im_1849	285	-	-	25-07-2020	overcast
flight-08	im_1850-im_2042	193	-	-	25-07-2020	overcast
flight-09	im_2043-im_2312	270	-	-	25-07-2020	overcast
flight-10	im_2313-im_2566	254	-	-	25-07-2020	overcast
flight-11	im_2567-im_2771	205	-	-	25-07-2020	overcast
flight-12	im_2772-im_2947	176	-	-	26-07-2020	overcast
flight-13	im_2948-im_3158	211	-	-	26-07-2020	overcast
flight-15	im_3159-im_3323	165	-	-	26-07-2020	overcast
flight-16	im_3324-im_3515	192	-	im_3502	08-08-2020	overcast
flight-17	im_3516-im_3729	214	-	-	08-08-2020	overcast
flight-18	im_3730-im_3964	235	-	-	08-08-2020	overcast
flight-19	im_3965-im_4202	238	-	-	09-08-2020	overcast
flight-20	im_4203-im_4385	183	-	im_4385	09-08-2020	overcast
flight-21	im_4386-im_4587	202	-	-	09-08-2020	overcast
flight-22	im_4588-im_4764	177	-	im_4750, im_4754	09-08-2020	overcast

flight	image-ids	image-count	disabled	non-aligned	flight-date	weather
flight-23	im_4765-im_5015	251	-	-	18-08-2020	mostly sunny
flight-24	im_5016-im_5267	252	-	-	18-08-2020	mostly sunny
flight-25	im_5268-im_5512	245	-	-	18-08-2020	mostly sunny

Table B1: Machine specifications of the machines used for the SfM photogrammetry processing.

No	Workstation type	Processor	Installed RAM	System Type	Windows Edition	Windows Version	OS-Build	Graphics card	Driver version	Metashape Version
AG-WS-Z6-01	HP Z6 G4	Intel® Xeon® Gold 5122 CPU @ 3.60GHz 3.59GHz	128 GB	64-bit	Windows 10 Enterprise	2004	19041,1110	NVIDIA Quadro P5000	27.21.14.5239	1.7.2.12040
AG-WS-Z6-02	HP Z1 Entry Tower G5	Intel® Core™ i9-9900K CPU @ 3.60GHz 3.60GHz	128 GB	64-bit	Windows 10 Enterprise	2004	19041,1110	NVIDIA GeForce RTX2080	27.21.14.6140	1.7.2.12040
AG-WS-Z6-03	HP Z1 Entry Tower G5	Intel® Core™ i9-9900K CPU @ 3.60GHz 3.60GHz	128 GB	64-bit	Windows 10 Enterprise	2004	19041,1110	NVIDIA GeForce RTX2080	27.21.14.5749	1.7.2.12040
AG-WS-Z1-01	HP Z1 Entry Tower G6	Intel® Core™ i9-10900K CPU @ 2.80GHz 2.81GHz	128 GB	64-bit	Windows 10 Enterprise	2004	19041,1110	NVIDIA GeForce RTX2080 SUPER		1.7.2.12040
AG-WS-Z1-02	HP Z1 Entry Tower G6	Intel® Core™ i9-10900K CPU @ 2.80GHz 2.81GHz	128 GB	64-bit	Windows 10 Enterprise	2004	19041,1110	NVIDIA GeForce RTX2080 SUPER		1.7.2.12040
AG-WS-Z1-03	HP Z1 Entry Tower G5	Intel® Core™ i9-9900K CPU @ 3.60GHz 3.60GHz	128 GB	64-bit	Windows 10 Enterprise	2004	19041,1052	NVIDIA GeForce RTX2080		1.7.2.12040

Table C1: Structural measurements and ground truthing of selected faults, acquired summer 2021. Easting and Northing given in the WGS 84/UTM zone 33N (EPSG:32633) projection. The calculated orthogonal heights use the Earth Gravitational Model 2008 (Pavlis et al., 2008).

Point_ID	Point_Role	Strike	Dip	Northing (y, m)	Easting (x, m)	Altitude (m)	DTM (m)	Alt.-DTM (cm)
KW-F0-STR_GPS0001	Code PP	-	-	8696460.286	518756.896	106.015	108.315	-229.947
KW-F0-STR_GPS0003	Code PP	-	-	8696458.301	518756.472	107.934	109.565	-163.173
KW-F0_GPS0001	Code PP	-	-	8696454.318	518754.515	111.002	112.414	-141.229
KW-F0_GPS0008	Code PP	-	-	8696328.256	518729.995	171.578	170.285	129.371
KW-F0_GPS0012	Code PP	-	-	8696457.052	518756.378	114.335	110.181	415.425
KW-F0_GPS0016-S341-D45	Code PP	-	-	8696333.236	518729.75	167.34	167.944	-60.439
KW-F0_STR009-D64W	Code PP	-	-	8696310.002	518727.444	178.038	178.73	-69.273
KW-F0_STR017-D51W	Code PP	-	-	8696327.254	518730.066	169.742	170.652	-91.034
KW-F10_GPS0002	Code PP	-	-	8696423.945	518718.28	146.282	146.463	-18.041
KW-F10_GPS0003	Code PP	-	-	8696416.604	518720.209	146.21	147.017	-80.614
KW-F1_GPS0004	Code PP	-	-	8696472.47	518729.793	134.386	133.863	52.314
KW-F2_GPS0002	Code PP	-	-	8696433.364	518731.923	135.549	135.367	18.184
KW-F3_STR012-DIP55NW	Code PP	-	-	8696270.747	518740.86	188.103	186.908	119.511
KW-F5_GPS0001	Code PP	-	-	8696293.142	518774.962	160.989	161.125	-13.593
KW-F5_GPS0003	Code PP	-	-	8696296.485	518768.454	164.148	164.321	-17.316
KW-F5_GPS0004	Code PP	-	-	8696292.058	518791.84	156.752	155.472	128.049
KW-F5_GPS0005	Code PP	-	-	8696334.989	518766.264	143.964	143.173	79.130
KW-F6_GPS0004	Code PP	-	-	8696242.727	518752.355	190.514	191.068	-55.325
KW-F7_GPS0004	Code PP	-	-	8696225.701	518771.544	190.349	190.142	20.668
Mean	Code PP	-	-	-	-	-	-	1.193
RMSE	Code PP	-	-	-	-	-	-	136.941
Std.	Code PP	-	-	-	-	-	-	140.688
KW-F0-STR_GPS0002	Widelane PP	-	-	8696459.482	518757.275	108.021	108.052	-3.127
KW-F0_GPS00015	Widelane PP	-	-	8696313.79	518728.98	176.296	176.881	-58.485
KW-F0_GPS0015	Widelane PP	-	-	8696342.655	518731.01	163.24	163.185	5.475
KW-F0_STR333-D22SW	Widelane PP	-	-	8696306.097	518738.723	175.82	175.552	26.789
KW-F0_STR341-D24W	Widelane PP	-	-	8696315.672	518736.399	172.592	172.883	-29.152
KW-F0_STR356-D42W	Widelane PP	-	-	8696298.749	518740.577	177.18	177.275	-9.530
KW-F10_GPS0001	Widelane PP	-	-	8696433.977	518714.811	146.192	145.978	21.336
KW-F10_GPS0004	Widelane PP	-	-	8696401.999	518723.62	147.474	147.935	-46.099
KW-F10_GPS0007	Widelane PP	-	-	8696370.324	518727.928	154.16	153.553	60.701
KW-F10_GPS0008	Widelane PP	-	-	8696363.545	518728.592	155.543	155.464	7.842
KW-F10_STR053-50	Widelane PP	-	-	8696383.281	518728.179	149.168	149.906	-73.824
KW-F4_GPS0006	Widelane PP	-	-	8696303.806	518756.864	170.092	170.147	-5.504
KW-F6_GPS0005	Widelane PP	-	-	8696241.224	518752.289	191.52	191.576	-5.594
KW-F7_GPS0002	Widelane PP	-	-	8696266.339	518796.147	166.891	166.776	11.461
KW-F7_GPS0005	Widelane PP	-	-	8696220.51	518766.392	191.298	191.651	-35.321

Point_ID	Point_Role	Strike	Dip	Northing (y, m)	Easting (x, m)	Altitude (m)	DTM (m)	Alt.-DTM (cm)
KW-F7_GPS0006	Widelane PP	-	-	8696217.741	518764.418	191.976	192.206	-23.005
KW-F8_GPS0001	Widelane PP	-	-	8696319.93	518745.222	166.139	166.704	-56.424
Mean	Widelane PP	-	-	-	-	-	-	-12.498
RMSE	Widelane PP	-	-	-	-	-	-	36.013
Std.	Widelane PP	-	-	-	-	-	-	34.815
KW-F0-STR_GPS0004	Fixed PP	-	-	8696456.68	518755.911	110.41	110.573	-16.291
KW-F0_GPS0002	Fixed PP	-	-	8696448.839	518753.157	114.356	114.496	-13.988
KW-F0_GPS0003	Fixed PP	-	-	8696428.921	518749.878	121.365	121.825	-45.971
KW-F0_GPS0004	Fixed PP	-	-	8696416.751	518746.036	127.935	128.161	-22.597
KW-F0_GPS0005	Fixed PP	-	-	8696408.444	518746.003	131.095	131.539	-44.376
KW-F0_GPS0006	Fixed PP	-	-	8696353.24	518731.143	158.998	159.174	-17.656
KW-F0_GPS0007	Fixed PP	-	-	8696333.499	518729.948	167.343	167.729	-38.622
KW-F0_GPS0009	Fixed PP	-	-	8696319.408	518730.681	173.372	173.61	-23.800
KW-F0_GPS0010	Fixed PP	-	-	8696313.883	518729.056	176.824	176.79	3.366
KW-F0_GPS0011	Fixed PP	-	-	8696310.289	518727.653	178.823	178.573	24.988
KW-F0_GPS0013	Fixed PP	-	-	8696373.355	518732.689	149.41	149.713	-30.339
KW-F0_GPS0014	Fixed PP	-	-	8696369.258	518730.092	152.292	152.576	-28.381
KW-F0_STR024-D26W	Fixed PP	-	-	8696319.071	518730.498	173.817	173.842	-2.541
KW-F10_STR340-36W	Fixed PP	-	-	8696391.481	518726.555	148.327	148.693	-36.602
KW-F1_GPS0001	Fixed PP	-	-	8696450.341	518750.221	116.281	116.481	-20.038
KW-F1_GPS0002	Fixed PP	-	-	8696455.901	518742.946	120.727	120.817	-9.016
KW-F1_GPS0003	Fixed PP	-	-	8696461.142	518737.744	125.291	125.401	-10.961
KW-F1_GPS0005	Fixed PP	-	-	8696474.471	518728.393	134.914	135.054	-14.025
KW-F2_GPS0001	Fixed PP	-	-	8696431.43	518743.998	125.197	125.32	-12.268
KW-F2_GPS0003	Fixed PP	-	-	8696431.626	518736.309	131.819	132.035	-21.666
KW-F3_GPS0001	Fixed PP	-	-	8696315.864	518736.276	172.559	172.844	-28.559
KW-F3_GPS0002	Fixed PP	-	-	8696303.056	518739.512	176.009	176.232	-22.324
KW-F3_GPS0003	Fixed PP	-	-	8696299.529	518740.468	176.935	177.009	-7.405
KW-F3_GPS0004	Fixed PP	-	-	8696283.223	518743.671	182.031	182.094	-6.304
KW-F3_GPS0005	Fixed PP	-	-	8696265.368	518739.263	188.907	189.154	-24.688
KW-F4_GPS0001	Fixed PP	-	-	8696326.876	518763.024	149.073	149.201	-12.733
KW-F4_GPS0002	Fixed PP	-	-	8696321.203	518761.815	153.853	153.968	-11.535
KW-F4_GPS0003	Fixed PP	-	-	8696311.897	518758.326	163.487	163.354	13.384
KW-F4_GPS0004	Fixed PP	-	-	8696306.988	518758.403	167.672	167.706	-3.372
KW-F4_GPS0005	Fixed PP	-	-	8696305.151	518757.505	169.132	169.226	-9.389
KW-F5_GPS0002	Fixed PP	-	-	8696296.34	518768.501	164.321	164.366	-4.436
KW-F6_GPS0001	Fixed PP	-	-	8696277.021	518785.938	165.738	165.861	-12.320
KW-F6_GPS0002	Fixed PP	-	-	8696276.514	518783.578	167.927	168.169	-24.236
KW-F6_GPS0003	Fixed PP	-	-	8696244.044	518752.62	190.219	190.548	-32.869
KW-F7_GPS0001	Fixed PP	-	-	8696269.317	518797.22	164.749	164.915	-16.572
KW-F7_GPS0003	Fixed PP	-	-	8696262.888	518794.998	168.751	168.882	-13.104
Mean	Fixed PP	-	-	-	-	-	-	-16.590
RMSE	Fixed PP	-	-	-	-	-	-	22.003
Std.	Fixed PP	-	-	-	-	-	-	14.659

Figure 2. Targeted area and control point and image acquisition locations. Images are grouped by acquisition date. GCP: ground control point; CP: check point. Background orthophoto is courtesy of Norwegian Polar Institute (2017). Map uses the WGS 84/UTM zone 33N (EPSG:32633) projection.
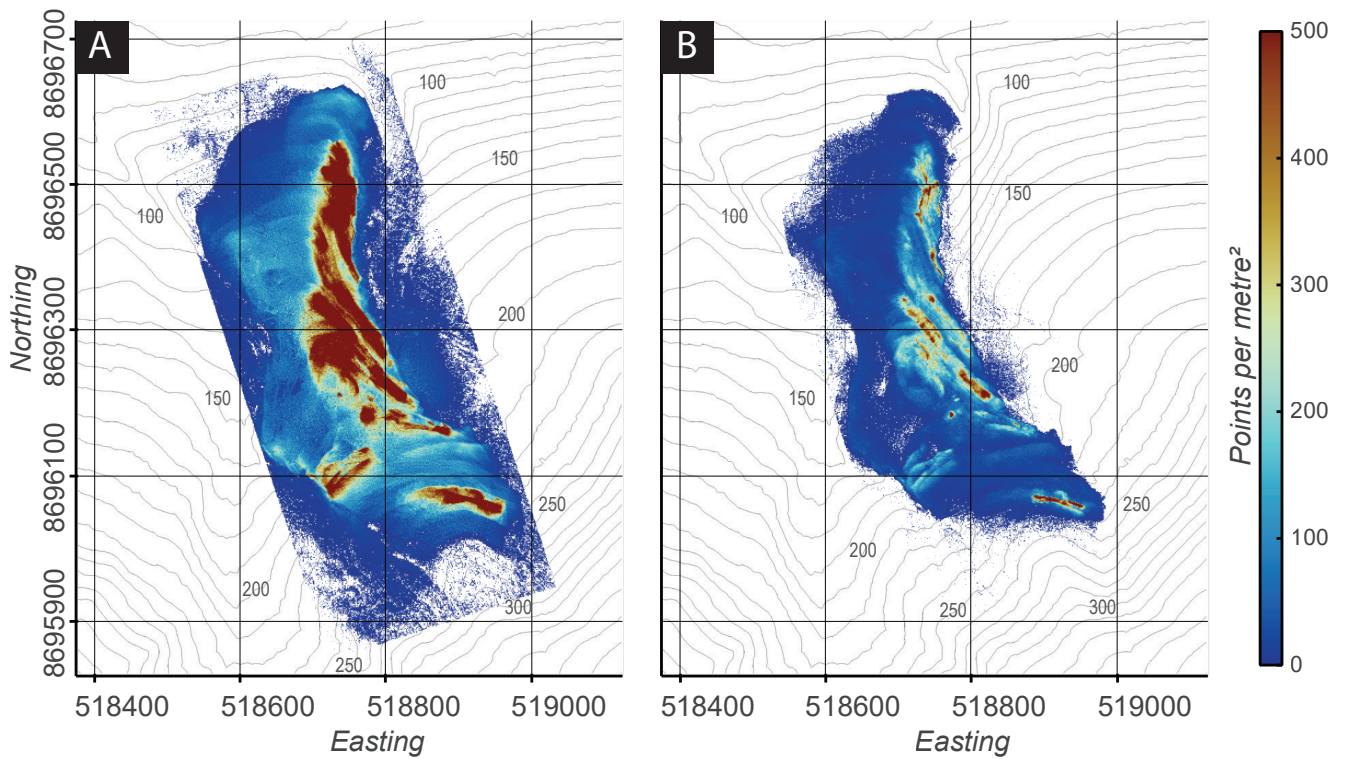
Figure 3. Sparse cloud point density maps, featuring both the raw tie-point set (A) and the optimized point cloud (B). Highest point densities are found close to control points and steeper sections. Maps use EPSG projection 32633. Contours generated from Norwegian Polar Institute (2014).
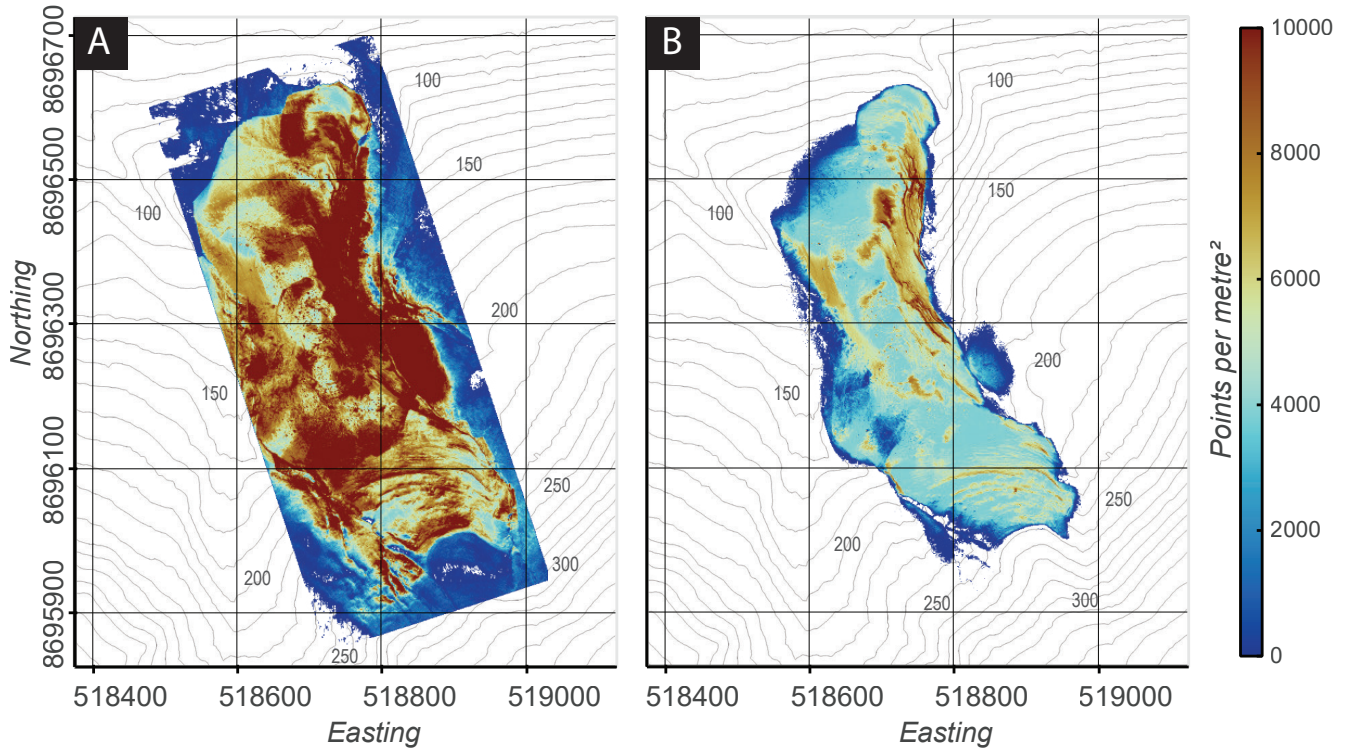
Figure 4. Dense cloud point density maps, featuring both the raw point set (A) and the confidence-filtered point cloud (B). Highest densities are found close to control points and steeper sections. Maps use EPSG projection 32633. Contours generated from Norwegian Polar Institute (2014).
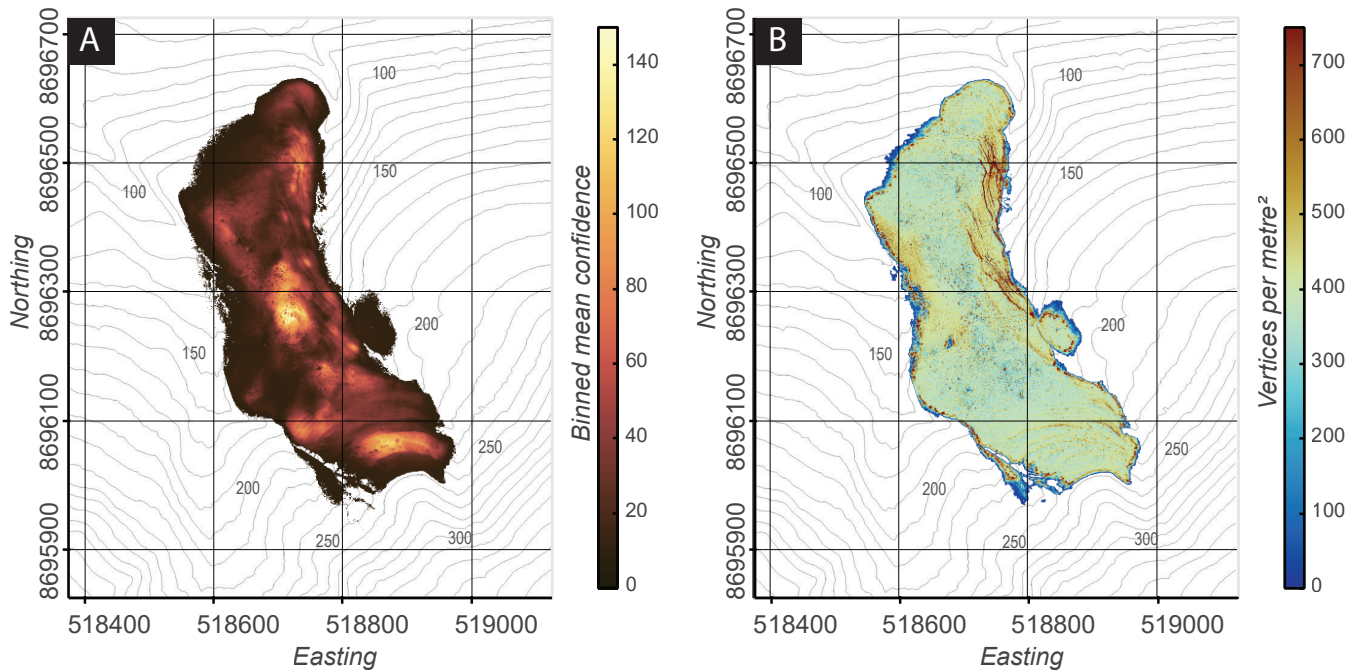
Figure 5. Dense cloud point confidence and mesh vertex density maps. The high-confidence dense cloud (A) was used as input for generation of the mesh (B) and other products. Maps use EPSG projection 32633. Contours generated from Norwegian Polar Institute (2014).
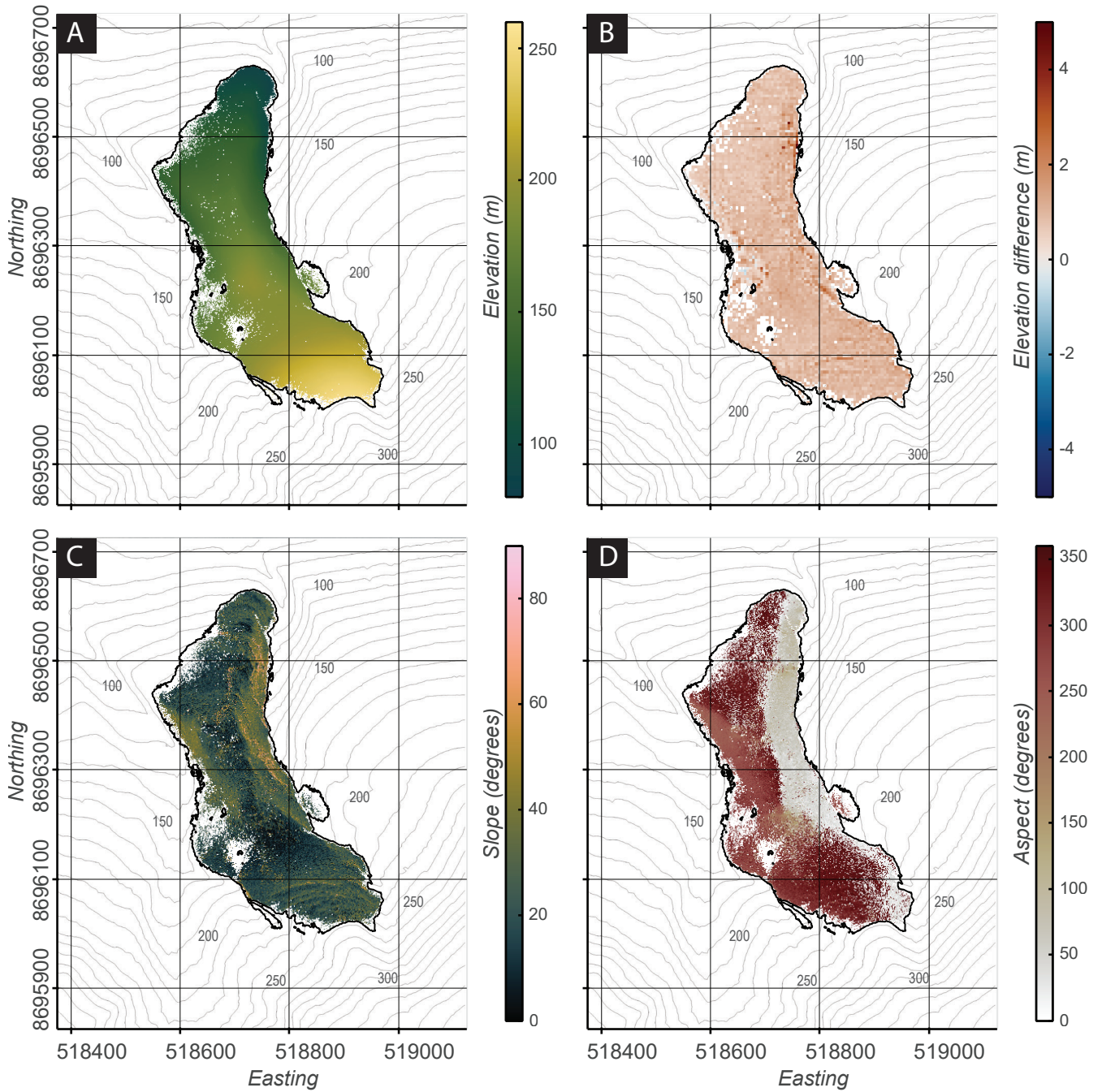
Figure 6. Digital Terrain Model (DTM) and related products. The difference between the Konusdalen West DTM and existing DTM reference data (Norwegian Polar Institute, 2014) is shown in B. Calculated slopes and aspect of the Konusdalen West exposure are shown in C and D, respectively. Maps use the WGS 84/UTM zone 33N (EPSG:32633) projection. Contours generated from Norwegian Polar Institute (2014).
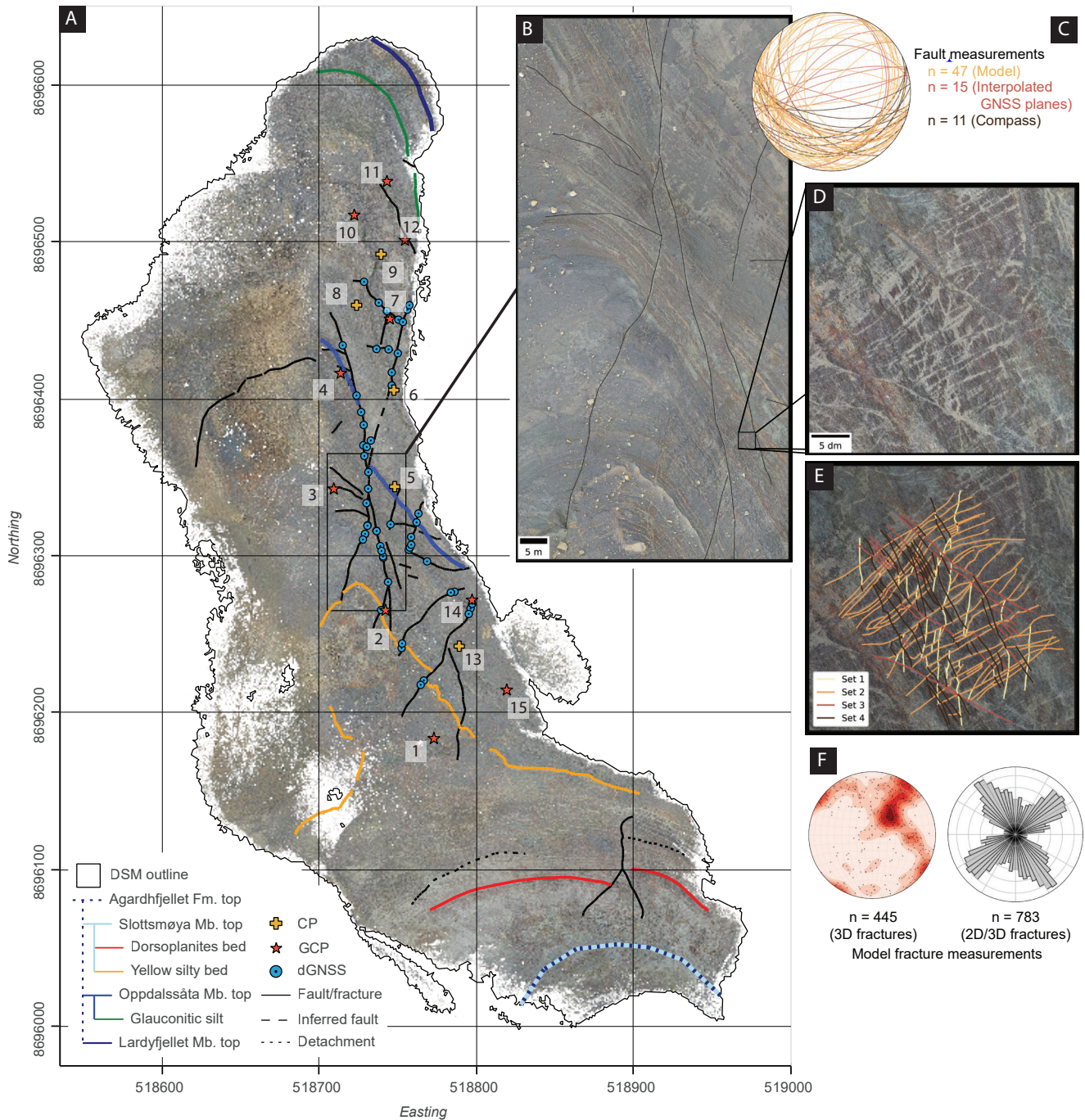
Figure 7. High resolution orthomosaics, stratigraphic units and structural measurements across the study area. A) Top-down view ortho-mosaic of the outcrop including control-point locations and basic interpretations. Control points are subdivided into dGNSS points, ground control points, and check points. B) The 50-by-100 m zoom-in shows the lower part of the Slottsmøya member, including major structural elements. C) Stereonet of field and model structural measurements of the faults. Compass measurements are supplemented by GNSS point-plane measurements and model measurements. D) The orthomosaic is of high enough resolution to identify and delineate sub-cm scale features, as the annotated fracture sets show in E). F) Stereonet of model-picked fractures from the sub-vertical part of the outcrop and rose diagram of model-picked fracture orientations across E). Only 3D/multi-segment fractures were included in the stereonet. Maps use the WGS 84/UTM zone 33N (EPSG:32633) projection.
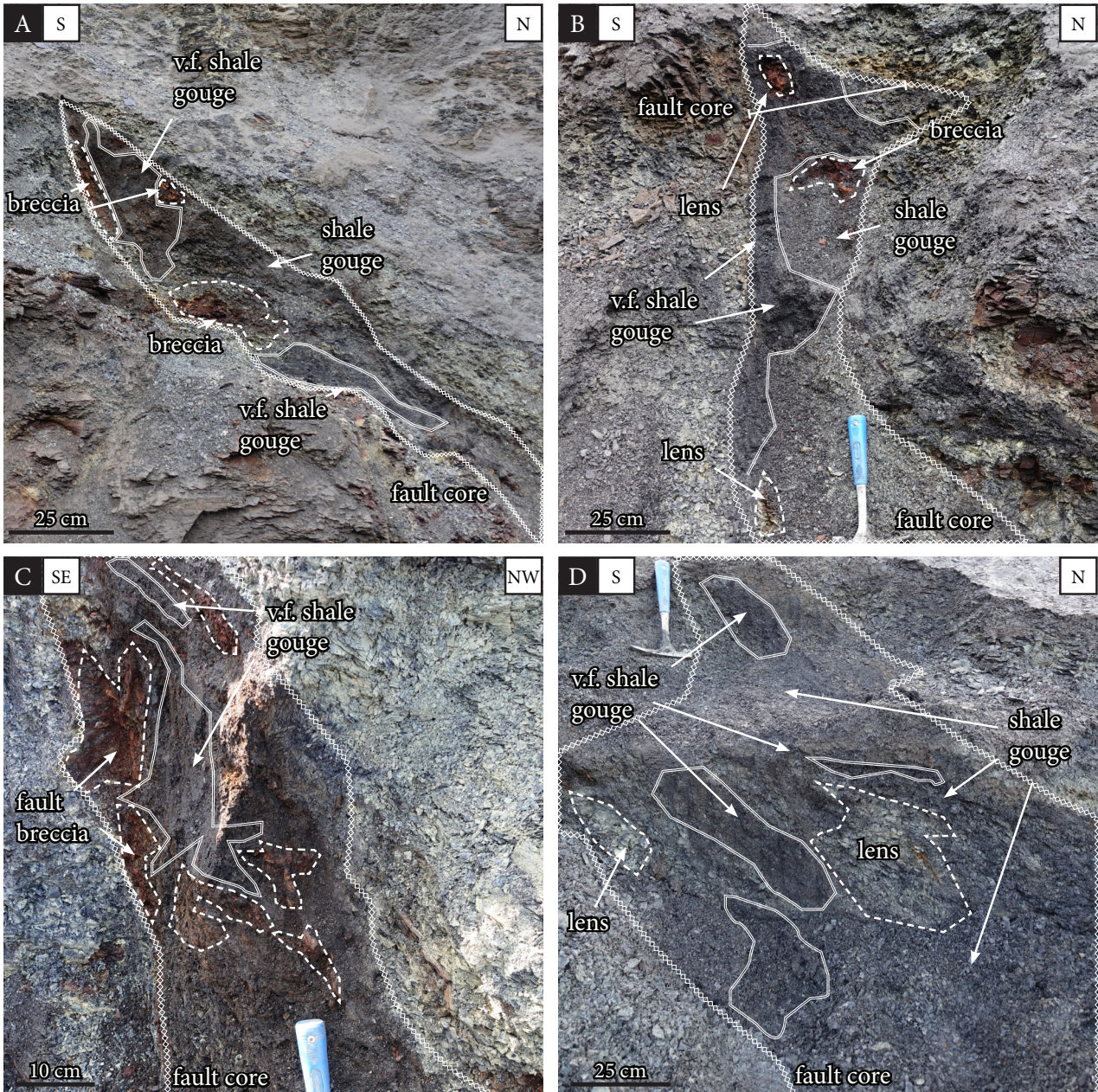
Figure 8. Fault core architectures at different points in the Konusdalen West outcrop. Fault core thickness varies depending on host rock lithology. Fault breccia and heavily fractured lenses are encompassed by fine to very fine shale membranes. Image locations are indicated in Fig. 9.
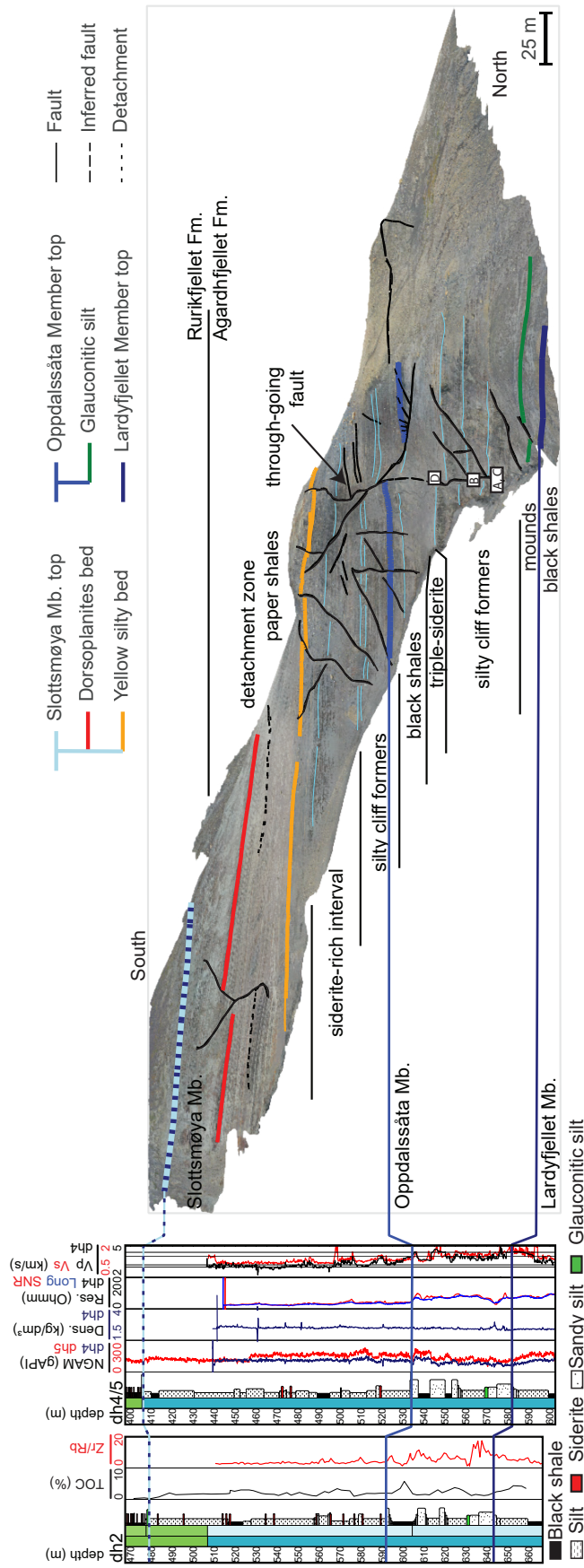
Figure 9. Side-view orthomosaic of the Konusdalen West DOM coupled with selected borehole data and borehole-outcrop integrations. Borehole data courtesy of the Longyearbyen CO$_2$ Lab, supplemented by data from Koevoets et al. (2018). A-D depict the locations of the images of Fig. 8.

Author contributions. PB: Conceptualization, Data curation, Formal analysis, Funding acquisition, Investigation, Methodology, Project administration, Software, Validation, Visualization, Writing - original draft preparation, Writing - review & editing; TB: Formal analysis, Investigation, Methodology, Validation, Writing - review & editing; GL: Formal analysis, Investigation, Validation, Writing - review & editing; SO: Formal analysis, Funding acquisition, Investigation, Methodology, Validation, Writing - review & editing; LN: Conceptualization, Funding acquisition, Investigation; KO: Conceptualization, Funding acquisition, Supervision, Visualization, Writing - review & editing; KS: Conceptualization, Funding acquisition, Supervision, Writing - review & editing.

Competing interests. The authors declare that they have no conflict of interest.

Acknowledgements. We sincerely appreciate the data provided by the UNIS CO_2 lab (http://CO2-ccs.unis.no/), and educational licenses provided by Schlumberger (Petrel), Cegal (Blueback plugins) and Advanced Logic Technology (WellCAD). We further thank our colleagues, in particularly Nil Rodes, Aleksandra Smyrak-Sikora, Julian Janocha, Richard Hann, and Karoline Løvlie, for meaningful discussions and their support during three extensive field campaigns, some plagued by polar bears. This study was partly funded by the Norwegian CCS Research Centre (NCCS; industry partners and The Research Council of Norway (RCN) #257579), and the Research Centre for Arctic Petroleum Exploration (ARCEx; industry partners and RCN #228107), in addition to three Svalbard Science Forum Arctic Field Grants (RCN #295627, #310638, and #322259). Finally, we thank David Tanner, Niklas W. Schaaf, an anonymous reviewer, and editor Kirsten Elger for constructive feedback that improved the original manuscript.

References

Barnes, R., Gupta, S., Traxler, C., Ortner, T., Bauer, A., Hesina, G., Paar, G., Huber, B., Juhart, K., Fritz, L., Nauschnegg, B., Muller, J.-P., and Tao, Y.: Geological Analysis of Martian Rover-Derived Digital Outcrop Models Using the 3-D Visualization Tool, Planetary Robotics 3-D Viewer-PRo3D, Earth and Space Science, 5, 285–307, https://doi.org/10.1002/2018EA000374, 2018.

Bergh, S. G., Braathen, A., and Andresen, A.: Interaction of Basement-Involved and Thin-Skinned Tectonism in the Tertiary Fold-Thrust Belt of Central Spitsbergen, Svalbard1, AAPG Bulletin, 81, 637–661, https://doi.org/10.1306/522B43F7-1727-11D7-8645000102C1865D, 1997.

Betlem, P.: Automated Metashape Package, Zenodo [code], https://doi.org/10.5281/zenodo.6448154, 2022a.

Betlem, P.: Svalbox-DOM_2020-0039, Norstore [data set], https://doi.org/10.11582/2022.00027, 2022b.

Betlem, P.: De-Risking Top Seal Integrity: Imaging Heterogeneity across Shale-Dominated Cap Rock Sequences, Ph.D. thesis, University of Oslo, Oslo, Norway, 2023a.

Betlem, P.: Svalbox-DOM_2020-0039: Supplementary Material and Processing Examples, Zenodo [code], https://doi.org/10.5281/zenodo.10182529, 2023b.

Betlem, P., Rodes, N., Birchall, T., Dahlin, A., Smyrak-Sikora, A., and Senger, K.: Svalbox Digital Model Database: A Geoscientific Window into the High Arctic, Geosphere, https://doi.org/10.1130/GES02606.1, 2023.

Bilmes, A., D'Elia, L., Lopez, L., Richiano, S., Varela, A., Alvarez, M. d. P., Bucher, J., Eymard, I., Muravchik, M., Franzese, J., and Ariztegui, D.: Digital Outcrop Modelling Using "Structure-from- Motion" Photogrammetry: Acquisition Strategies, Validation and Interpretations to Different Sedimentary Environments, Journal of South American Earth Sciences, 96, 102 325, https://doi.org/10.1016/j.jsames.2019.102325, 2019.

Birchall, T., Senger, K., Hornum, M., Olaussen, S., and Braathen, A.: Underpressure of the Barents Shelf: Causes and Implications for Hydrocarbon Exploration, AAPG Bulletin, https://doi.org/10.1306/02272019146, 2020.

Braathen, A., Bergh, S. G., and Maher Jr., H. D.: Structural Outline of a Tertiary Basement-cored Uplift/Inversion Structure in Western Spitsbergen, Svalbard: Kinematics and Controlling Factors, Tectonics, 14, 95–119, https://doi.org/10.1029/94TC01677, 1995.

Braathen, A., Berc, S. G., and Maher, H. D.: Thrust Kinematics in the Central Part of the Tertiary Transpressional Fold-Thrust Belt in Spitsbergen, Geological Survey of Norway, 433, 32–33, 1997.

Braathen, A., Bælum, K., Christiansen, H. H., Dahl, T., Eiken, O., Elvebakk, H., Hansen, F., Hanssen, T. H., Jochmann, M., and Johansen, T. A.: The Longyearbyen CO2 Lab of Svalbard, Norway-initial Assessment of the Geological Conditions for CO2 Sequestration, Norwegian Journal of Geology, 92, 353–376, 2012.

Bradski, G.: The OpenCV Library, Dr. Dobb's Journal: Software tools for the Professional Programmer, 25, 120–123, 2000.

Buckley, S. J., Ringdal, K., Naumann, N., Dolva, B., Kurz, T. H., Howell, J. A., and Dewez, T. J.: LIME: Software for 3-D Visualization, Interpretation, and Communication of Virtual Geoscience Models, Geosphere, 15, 222–235, https://doi.org/10.1130/GES02002.1, 2019.

Buckley, S. J., Howell, J. A., Naumann, N., Lewis, C., Chmielewska, M., Ringdal, K., Vanbiervliet, J., Tong, B., Mulelid-Tynes, O. S., Foster, D., Maxwell, G., and Pugsley, J.: V3Geo: A Cloud-Based Repository for Virtual 3D Models in Geoscience, Geoscience Communication, 5, 67–82, https://doi.org/10.5194/gc-5-67-2022, 2022.

Burnham, B. S., Bond, C., Flaig, P. P., van der Kolk, D. A., and Hodgetts, D.: Outcrop Conservation: Promoting Accessibility, Inclusivity, and Reproducibility through Digital Preservation, The Sedimentary Record, 20, 5–14, 2022.

Butler, H., Chambers, B., Hartzell, P., and Glennie, C.: PDAL: An Open Source Library for the Processing and Analysis of Point Clouds, Computers & Geosciences, 148, 104 680, https://doi.org/10.1016/j.cageo.2020.104680, 2021.

Cawood, A. J. and Bond, C. E.: eRock: An Open-Access Repository of Virtual Outcrops for Geoscience Education, GSA today, 28, 36–37, 2019.

Collignon, M. and Hammer, Ø.: Petrography and Sedimentology of the Slottsmøya Member at Janusfjellet, Central Spitsbergen., Norwegian Journal of Geology, 92, 89–101, 2012.

Crameri, F., Shephard, G. E., and Heron, P. J.: The Misuse of Colour in Science Communication, Nature Communications, 11, 5444, https://doi.org/10.1038/s41467-020-19160-7, 2020.

Dering, G. M., Micklethwaite, S., Thiele, S. T., Vollgger, S. A., and Cruden, A. R.: Review of Drones, Photogrammetry and Emerging Sensor Technology for the Study of Dykes: Best Practises and Future Potential, Journal of Volcanology and Geothermal Research, 373, 148–166, https://doi.org/10.1016/j.jvolgeores.2019.01.018, 2019.

Donnadieu, F., Kelfoun, K., van Wyk de Vries, B., Cecchi, E., and Merle, O.: Digital Photogrammetry as a Tool in Analogue Modelling: Applications to Volcano Instability, Journal of Volcanology and Geothermal Research, 123, 161–180, https://doi.org/10.1016/S0377-0273(03)00034-9, 2003.

Dypvik, H. and Harris, N. B.: Geochemical Facies Analysis of Fine-Grained Siliciclastics Using Th/U, Zr/Rb and (Zr+Rb)/Sr Ratios, Chemical Geology, 181, 131–146, https://doi.org/10.1016/S0009-2541(01)00278-9, 2001.

Dypvik, H., Eikeland, T. A., Backer-Owe, K., Andresen, A., Johanen, H., Elverhøi, A., Nagy, J., Haremo, P., and Biærke, T.: The Janusfjellet Subgroup (Bathonian to Hauterivian) on Central Spitsbergen: A Revised Lithostratigraphy, Polar Research, 9, 21–44, https://doi.org/10.1111/j.1751-8369.1991.tb00400.x, 1991.

Garrido-Jurado, S., Muñoz-Salinas, R., Madrid-Cuevas, F. J., and Marín-Jiménez, M. J.: Automatic Generation and Detection of Highly Reliable Fiducial Markers under Occlusion, Pattern Recognition, 47, 2280–2292, https://doi.org/10.1016/j.patcog.2014.01.005, 2014.

Grundvåg, S. A., Marin, D., Kairanov, B., Śliwińska, K. K., Nøhr-Hansen, H., Jelby, M. E., Escalona, A., and Olaussen, S.: The Lower Cretaceous Succession of the Northwestern Barents Shelf: Onshore and Offshore Correlations, Marine and Petroleum Geology, 86, 834–857, https://doi.org/10.1016/j.marpetgeo.2017.06.036, 2017.

Harland, W. B., Anderson, L. M., Manasrah, D., Butterfield, N. J., Challinor, A., Doubleday, P. A., Dowdeswell, E. K., Dowdeswell, J. A., Geddes, I., Kelly, S. R., Lesk, E. L., Spencer, A. M., and Stephens, C. F.: The Geology of Svalbard, vol. 17, Geological Society London, London, 1997.

Harrald, J. E. G., Coe, A. L., Thomas, R. M., and Hoggett, M.: Use of Drones to Analyse Sedimentary Successions Exposed in the Foreshore, Proceedings of the Geologists' Association, 132, 253–268, https://doi.org/10.1016/j.pgeola.2021.02.001, 2021.

Healy, D., Rizzo, R. E., Cornwell, D. G., Farrell, N. J. C., Watkins, H., Timms, N. E., Gomez-Rivas, E., and Smith, M.: FracPaQ: A MATLAB™ Toolbox for the Quantification of Fracture Patterns, Journal of Structural Geology, 95, 1–16, https://doi.org/10.1016/j.jsg.2016.12.003, 2017.

Henriksen, E., Ryseth, A. E., Larssen, G. B., Heide, T., Rønning, K., Sollid, K., and Stoupakova, A. V.: Chapter 10 Tectonostratigraphy of the Greater Barents Sea: Implications for Petroleum Systems, Geological Society, London, Memoirs, 35, 163–195, https://doi.org/10.1144/M35.10, 2011.

Hiep, V. H., Keriven, R., Labatut, P., and Pons, J.-P.: Towards High-Resolution Large-Scale Multi-View Stereo, in: IEEE Conference on Computer Vision and Pattern Recognition (20-25 June 2009), pp. 1430–1437, IEEE, Miami, FL, USA, 2009.

Hirschmuller, H.: Stereo Processing by Semiglobal Matching and Mutual Information, IEEE Transactions on pattern analysis and machine intelligence, 30, 328–341, 2007.

Hodgetts, D., Seers, T., Head, W., and Burnham, B. S.: High Performance Visualisation of Multiscale Geological Outcrop Data in Single Software Environment, in: 77th EAGE Conference and Exhibition 2015, vol. 2015, pp. 1–5, European Association of Geoscientists & Engineers, Madrid, Spain, https://doi.org/10.3997/2214-4609.201412862, 2015.

Howell, J. A., Martinius, A. W., and Good, T. R.: The Application of Outcrop Analogues in Geological Modelling: A Review, Present Status and Future Outlook, Geological Society, London, Special Publications, 387, 1–25, https://doi.org/10.1144/SP387.12, 2014.

Humlum, O., Instanes, A., and Sollid, J. L.: Permafrost in Svalbard: A Review of Research History, Climatic Background and Engineering Challenges, Polar Research, 22, 191–215, https://doi.org/10.1111/j.1751-8369.2003.tb00107.x, 2003.

Huq, F., Smalley, P. C., Mørkved, P. T., Johansen, I., Yarushina, V., and Johansen, H.: The Longyearbyen CO2 Lab: Fluid Communication in Reservoir and Caprock, International Journal of Greenhouse Gas Control, 63, 59–76, https://doi.org/10.1016/j.ijggc.2017.05.005, 2017.

James, M. R., Chandler, J. H., Eltner, A., Fraser, C., Miller, P. E., Mills, J. P., Noble, T., Robson, S., and Lane, S. N.: Guidelines on the Use of Structure-from-Motion Photogrammetry in Geomorphic Research, Earth Surface Processes and Landforms, 44, 2081–2084, https://doi.org/10.1002/esp.4637, 2019.

Kingsland, K.: Comparative Analysis of Digital Photogrammetry Software for Cultural Heritage, Digital Applications in Archaeology and Cultural Heritage, 18, e00 157, https://doi.org/10.1016/j.daach.2020.e00157, 2020.

Koevoets, M. J., Abay, T. B., Hammer, Ø., and Olaussen, S.: High-Resolution Organic Carbon–Isotope Stratigraphy of the Middle Jurassic–Lower Cretaceous Agardhfjellet Formation of Central Spitsbergen, Svalbard, Palaeogeography, Palaeoclimatology, Palaeoecology, 449, 266–274, https://doi.org/10.1016/j.palaeo.2016.02.029, 2016.

Koevoets, M. J., Hammer, Ø., Olaussen, S., Senger, K., and Smelror, M.: Integrating Subsurface and Outcrop Data of the Middle Jurassic to Lower Cretaceous Agardhfjellet Formation in Central Spitsbergen, Norwegian Journal of Geology, 98, https://doi.org/10.17850/njg98-4-01, 2018.

Koevoets, M. K., Hammer, Ø., and Little, C. T. S.: Palaeoecology and Palaeoenvironments of the Middle Jurassic to Lowermost Cretaceous Agardhfjellet Formation (Bathonian-Ryazanian), Spitsbergen, Svalbard, Norwegian Journal of Geology, 99, 2019.

Leica Geosystems AG: Leica Viva GS16 Data Sheet, 2016.

Leon, J. X., Heuvelink, G. B. M., and Phinn, S. R.: Incorporating DEM Uncertainty in Coastal Inundation Mapping, PLOS ONE, 9, e108 727, https://doi.org/10.1371/journal.pone.0108727, 2014.

Løvlie, K. H.: Structural Deformation and Mineralogy of the Agardhfjellet and Rurikfjellet Formations in Central Spitsbergen, Svalbard, MSc, University of Oslo, Oslo, 2020.

Marques, A., Horota, R. K., de Souza, E. M., Kupssinskü, L., Rossa, P., Aires, A. S., Bachi, L., Veronez, M. R., Gonzaga, L., and Cazarin, C. L.: Virtual and Digital Outcrops in the Petroleum Industry: A Systematic Review, Earth-Science Reviews, 208, 103 260, https://doi.org/10.1016/j.earscirev.2020.103260, 2020.

Mørk, A., Dallmann, W. K., Dypvik, H., Johannessen, E. P., Larssen, G. B., Nagy, J., Nøttvedt, A., Olaussen, S., Pchelina, T. M., and Worsley, D.: Mesozoic Lithostratigraphy, Lithostratigraphic lexicon of Svalbard. Upper Palaeozoic to Quaternary bedrock. Review and recommendations for nomenclature use, pp. 127–214, 1999.

Mulrooney, M. J., Larsen, L., Van Stappen, J. F., Rismyhr, B., Senger, K., Braathen, A., Olaussen, S., Mørk, M. B. E., Ogata, K., and Cnudde, V.: Fluid Flow Properties of the Wilhelmøya Subgroup, a Potential Unconventional CO2 Storage Unit in Central Spitsbergen, Norwegian Journal of Geology, 99, 85–116, https://doi.org/10.17850/njg002, 2018.

Nakken, L.: Structural Evolution of the Lower Agardhfjellet Formation, in Central Spitsbergen: Implications for Caprock Integrity, MSc, University of Oslo, Oslo, Norway, 2020.

Norwegian Polar Institute: Terrengmodell Svalbard (S0 Terrengmodell), https://doi.org/10.21334/NPOLAR.2014.DCE53A47, 2014.

Norwegian Polar Institute: Geological Map of Svalbard (1:250000), https://doi.org/10.21334/NPOLAR.2016.616F7504, 2016.

Norwegian Polar Institute: NP_Ortofoto_Svalbard_WMTS_25833 [Dataset], 2017.

Nyberg, B., Nixon, C. W., and Sanderson, D. J.: NetworkGT: A GIS Tool for Geometric and Topological Analysis of Two-Dimensional Fracture Networks, Geosphere, 14, 1618–1634, https://doi.org/10.1130/GES01595.1, 2018.

Ogata, K., Senger, K., Braathen, A., Tveranger, J., and Olaussen, S.: The Importance of Natural Fractures in a Tight Reservoir for Potential CO2 Storage: A Case Study of the Upper Triassic-middle Jurassic Kapp Toscana Group (Spitsbergen, Arctic Norway), Geological Society, London, Special Publications, 374, 395–415, https://doi.org/10.1144/SP374.9, 2012.

Ogata, K., Senger, K., Braathen, A., Tveranger, J., and Olaussen, S.: Fracture Systems and Mesoscale Structural Patterns in the Siliciclastic Mesozoic Reservoir-Caprock Succession of the Longyearbyen CO2 Lab Project: Implications for Geological CO2 Sequestration in Central Spitsbergen, Svalbard, Norwegian Journal of Geology, 94, 121–154, 2014.

Ogata, K., Weert, A., Betlem, P., Birchall, T., and Senger, K.: Shallow and Deep Subsurface Sediment Remobilization and Intrusion in the Middle Jurassic to Lower Cretaceous Agardhfjellet Formation (Svalbard), Geosphere, 19, 801–822, https://doi.org/10.1130/GES02555.1, 2023.

Olaussen, S., Senger, K., Braathen, A., Grundvåg, S.-A., and Mørk, A.: You Learn as Long as You Drill; Research Synthesis from the Longyearbyen CO2 Laboratory, Svalbard, Norway., Norwegian Journal of Geology, 99, 157–188, https://doi.org/10.17850/njg008, 2019.

Over, J.-S. R., Ritchie, A. C., Kranenburg, C. J., Brown, J. A., Buscombe, D. D., Noble, T., Sherwood, C. R., Warrick, J. A., and Wernette, P. A.: Processing Coastal Imagery with Agisoft Metashape Professional Edition, Version 1.6-Structure from Motion Workflow Documentation, Tech. rep., US Geological Survey, 2021.

Pavlis, N., Kenyon, S., Factor, J., and Holmes, S.: Earth Gravitational Model 2008, in: SEG Technical Program Expanded Abstracts 2008, SEG Technical Program Expanded Abstracts, pp. 761–763, Society of Exploration Geophysicists, Tulsa, Olkahoma, https://doi.org/10.1190/1.3063757, 2008.

PDAL Contributors: PDAL Point Data Abstraction Library, Zenodo [code], https://doi.org/10.5281/zenodo.2556738, 2018.

Rippin, D. M., Pomfret, A., and King, N.: High Resolution Mapping of Supra-Glacial Drainage Pathways Reveals Link between Micro-Channel Drainage Density, Surface Roughness and Surface Reflectance, Earth Surface Processes and Landforms, 40, 1279–1290, https://doi.org/10.1002/esp.3719, 2015.

Rizzo, R., Forbes Inskip, N., Fazeli, H., Betlem, P., Bisdom, K., Kampman, N., Snippe, J., Senger, K., Doster, F., and Busch, A.: Modelling Geological Co2 Leakage: Integrating Fracture Permeability and Fault Zone Outcrop Analysis, https://doi.org/10.2139/ssrn.4571419, 2023.

Rizzo, R. E., Fazeli, H., Maier, C., March, R., Egya, D., Doster, F., Kubeyev, A., Kampman, N., Bisdom, K., Snippe, J., Senger, K., Betlem, P., Phillips, T., Inskip, N. F., Esegbue, O., and Busch, A.: Understanding Fault and Fracture Networks to De-Risk Geological Leakage from Subsurface Storage Sites, in: 1st Geoscience & Engineering in Energy Transition Conference, vol. 2020, pp. 1–5, European Association of Geoscientists & Engineers, Strasbourg, France, https://doi.org/10.3997/2214-4609.202021016, 2020.

Rizzo, R. E., Fazeli, H., Doster, F., Kampman, N., Bisdom, K., Snippe, J., Senger, K., Betlem, P., and Busch, A.: Role of Fault and Fracture Networks to De-Risk Geological Leakage from Subsurface Energy Sites, in: EGU General Assembly 2021, pp. EGU21–8517, Online, https://doi.org/10.5194/egusphere-egu21-8517, 2021.

Rouault, E., Warmerdam, F., Schwehr, K., Kiselev, A., Butler, H., Łoskot, M., Szekeres, T., Tourigny, E., Landa, M., Miara, I., Elliston, B., Kumar, C., Plesea, L., Morissette, D., Jolma, A., and Dawson, N.: GDAL, Zenodo [code], https://doi.org/10.5281/zenodo.6352176, 2022.

Schaaf, N. W., Senger, K., Mulrooney, M. J., Ogata, K., Braathen, A., and Olaussen, S.: Towards Characterization of Natural Fractures in a Caprock Shale: An Integrated Borehole-Outcrop Study of the Agardhfjellet For-mation, Svalbard, Arctic Norway, in: Norwegian Geological Society Winter Conference, Oslo, https://doi.org/10.13140/RG.2.2.23744.74249/1, 2017.

Senger, K., Tveranger, J., Ogata, K., Braathen, A., and Planke, S.: Late Mesozoic Magmatism in Svalbard: A Review, Earth-Science Reviews, 139, 123–144, https://doi.org/10.1016/j.earscirev.2014.09.002, 2014.

Senger, K., Buckley, S. J., Chevallier, L., Fagereng, Å., Galland, O., Kurz, T. H., Ogata, K., Planke, S., and Tveranger, J.: Fracturing of Doleritic Intrusions and Associated Contact Zones: Implications for Fluid Flow in Volcanic Basins, Journal of African Earth Sciences, 102, 70–85, https://doi.org/10.1016/j.jafrearsci.2014.10.019, 2015.

Senger, K., Brugmans, P., Grundvåg, S.-A., Jochmann, M., Nøttvedt, A., Olaussen, S., Skotte, A., and Smyrak-Sikora, A.: Petroleum, Coal and Research Drilling Onshore Svalbard: A Historical Perspective, Norwegian Journal of Geology, 99, https://doi.org/10.17850/njg99-3-1, 2019.

Sibson, R. H.: Structural Permeability of Fluid-Driven Fault-Fracture Meshes, Journal of Structural Geology, 18, 1031–1042, https://doi.org/10.1016/0191-8141(96)00032-6, 1996.

Smith, M., Carrivick, J., and Quincey, D.: Structure from Motion Photogrammetry in Physical Geography, Progress in Physical Geography: Earth and Environment, 40, 247–275, https://doi.org/10.1177/0309133315615805, 2016.

Spencer, A. M., Briskeby, P. I., Christensen, L. D., Foyn, R., Kjolleberg, M., Kvadsheim, E., Knight, I., Rye-Larsen, M., and Williams, J.: Petroleum Geoscience in Norden-exploration, Production and Organization, Episodes, 31, 115–124, 2008.

Stevens, J.-L. R., Rudiger, P., and Bednar, J. A.: HoloViews: Building Complex Visualizations Easily for Reproducible Science, in: Proceedings of the 14th Python in Science Conference, pp. 61–69, Citeseer, 2015.

Tinkham, W. T. and Swayze, N. C.: Influence of Agisoft Metashape Parameters on UAS Structure from Motion Individual Tree Detection from Canopy Height Models, Forests, 12, 250, https://doi.org/10.3390/f12020250, 2021.

Tonkin, T. N., Midgley, N. G., Cook, S. J., and Graham, D. J.: Ice-Cored Moraine Degradation Mapped and Quantified Using an Unmanned Aerial Vehicle: A Case Study from a Polythermal Glacier in Svalbard, Geomorphology, 258, 1–10, https://doi.org/10.1016/j.geomorph.2015.12.019, 2016.

Vieira, G., Mora, C., Pina, P., Ramalho, R., and Fernandes, R.: UAV-based Very High Resolution Point Cloud, Digital Surface Model and Orthomosaic of the Chã Das Caldeiras Lava Fields (Fogo, Cabo Verde), Earth System Science Data, 13, 3179–3201, https://doi.org/10.5194/essd-13-3179-2021, 2021.

Vollgger, S. A. and Cruden, A. R.: Mapping Folds and Fractures in Basement and Cover Rocks Using UAV Photogrammetry, Cape Liptrap and Cape Paterson, Victoria, Australia, Journal of Structural Geology, 85, 168–187, https://doi.org/10.1016/j.jsg.2016.02.012, 2016.

Westoby, M. J., Brasington, J., Glasser, N. F., Hambrey, M. J., and Reynolds, J. M.: 'Structure-from-Motion' Photogrammetry: A Low-Cost, Effective Tool for Geoscience Applications, Geomorphology, 179, 300–314, https://doi.org/10.1016/j.geomorph.2012.08.021, 2012.

Wilkinson, M. D., Dumontier, M., Aalbersberg, I. J., Appleton, G., Axton, M., Baak, A., Blomberg, N., Boiten, J.-W., da Silva Santos, L. B., Bourne, P. E., Bouwman, J., Brookes, A. J., Clark, T., Crosas, M., Dillo, I., Dumon, O., Edmunds, S., Evelo, C. T., Finkers, R., Gonzalez-Beltran, A., Gray, A. J. G., Groth, P., Goble, C., Grethe, J. S., Heringa, J., 't Hoen, P. A. C., Hooft, R., Kuhn, T., Kok, R., Kok, J., Lusher, S. J., Martone, M. E., Mons, A., Packer, A. L., Persson, B., Rocca-Serra, P., Roos, M., van Schaik, R., Sansone, S.-A., Schultes, E., Sengstag, T., Slater, T., Strawn, G., Swertz, M. A., Thompson, M., van der Lei, J., van Mulligen, E., Velterop, J., Waagmeester, A., Wittenburg, P., Wolstencroft, K., Zhao, J., and Mons, B.: The FAIR Guiding Principles for Scientific Data Management and Stewardship, Scientific Data, 3, 160 018, https://doi.org/10.1038/sdata.2016.18, 2016.

Zhou, Y., Daakir, M., Rupnik, E., and Pierrot-Deseilligny, M.: A Two-Step Approach for the Correction of Rolling Shutter Distortion in UAV Photogrammetry, ISPRS Journal of Photogrammetry and Remote Sensing, 160, 51–66, https://doi.org/10.1016/j.isprsjprs.2019.11.020, 2020.